Simulation of RadioAstron Gravitational Redshift Experiment Accuracy

G. Granato
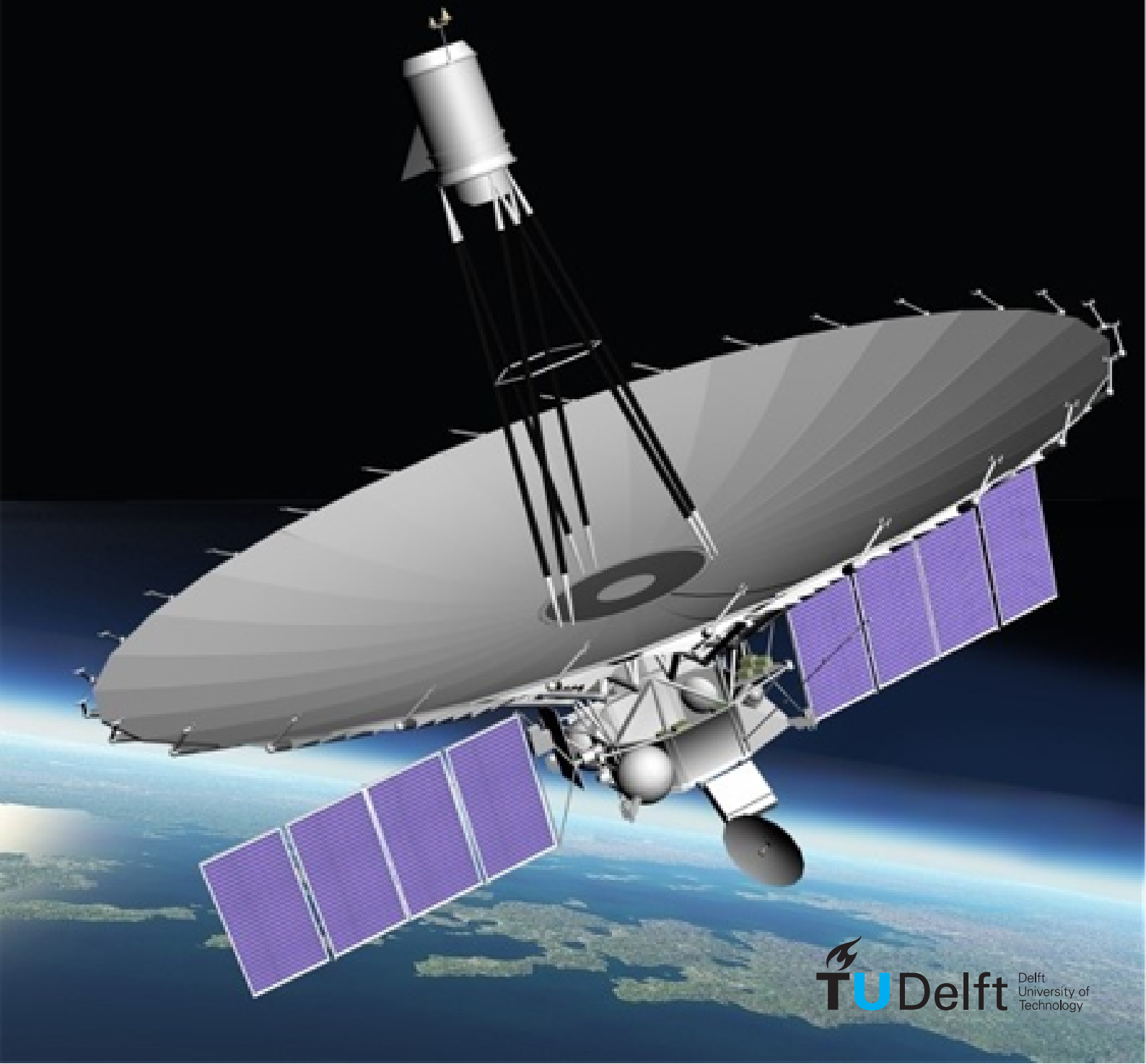
Simulation of RadioAstron Gravitational Redshift Experiment Accuracy

by

Giovanni Granato

(Student number: 4510607)

to obtain the degree of

Master of Science
in Aerospace Engineering

at the Delft University of Technology,
to be defended on Wednesday February 20, 2019 at 14:00

In support of the RadioAstron Gravitational Redshift Experiment

Supervisors

Dr. Ir. Dominic Dirkx	Prof. Dr. Leonid Gurvits
Astrodynamics and Space Missions	Head of Space Science and Innovative Applications Group, JIVE
TU Delft	Astrodynamics and Space Missions, TU Delft

TUDelft
Delft
University of
Technology

Acknowledgements

I would first like to thank my supervisors Dr. Ir. Dominic Dirkx and Prof. Dr. Leonid Gurvits very deeply and sincerely for giving me the opportunity to work on the extremely fascinating and challenging topic of the RadioAstron gravitational redshift experiment, becoming part of the research team. Since the very beginning they have been guiding and supported me with passionate participation throughout the several phases of the internship, literature study and thesis. Im very grateful to them for their infinite patience, advice, care, understanding and for supporting me in overcoming my difficult periods and obstacles I have been facing in my work: their help has been really precious and crucial for me.

Having the possibility to work on an actual ongoing experiment, even touching real data with my hands when I was in Finland, has been an enormous privilege for me. I am really grateful to Dr. Guifré Molera Calvés for his supervision and very useful tips during my four-month internship at Aalto University in Espoo, Finland, as well as Professor Esa Kallio who allowed me to work there.

I would like to thank all the members of the RadioAstron team for the important suggestions that they have given me, for sharing relevant information and their time during the development of the experiment. In particular PI Dmitry Litvinov and Mikhail Zakhvatkin for providing me with real experiment data and giving me good advice. Special thanks also to Prof. Norbert Bartel and Nelson Nunes who have given a significant contribution to the data processing supplying important results.

I would like to thank my parents and my family for their continuous support throughout my MSc years and for giving me the wonderful opportunity to study abroad and live this amazing, life changing and inestimable experience. I also thank my cousin Dario for his encouragement and affection. During my MSc study course and internship I have met amazing people to whom I will always be grateful for making this time special and unforgettable. I thank in particular my university friends and the people from the 'Bombers' group, as well as my old friends from Napoli and those from my hometown, in particular Michele and my martial arts school teacher Vincenzo who have always supported me in my life and studies.

I am greatly honoured to give my contribution to this amazing scientific research.

"Once we accept our limits, we go beyond them"
Albert Einstein

Contents

List of Figures

List of Tables

List of Symbols

Table 1: *List of Abbreviations and Symbols*

Acronym	Definition
Ma	Matera radio telescope
Wz	Wettzell radio telescope
Ys	Yebes radio telescope
Pu	Pushchino station
On	Onsala radio telescope
Hh	Hartbeesthoek radio telescope (26 m)
Ht	Hartbeesthoek radio telescope (15 m)
Sv	Svetloe radio telescope
Zc	Zelenchukskaya radio telescope
Bd	Badary radio telescope
Ww	Warkworth radio telescope
Yg	Yarragade radio telescope
Wn	Wettzell Nord radio telescope
PI	Principal Investigator
FFT	Fast Fourier Transform
VLBI	Very Long Baseline Interferometry
RA	RadioAstron
PRIDE	Planetary Radio Interferometry and Doppler Effect
EEP	Einstein Equivalence Principle
OD	Orbit Determination
GHM	Ground-based H-maser
SHM	Space-borne H-maser
SLR	Satellite Laser Ranging
SRP	Solar Radiation Pressure
ST	Stabilization Thrusters
TS	Tracking Station
f	Frequency
ϕ	phase
T	Averaging time
ε	EEP violation parameter

Summary

The RadioAstron Gravitational Redshift experiment aims to test the Einstein Equivalence Principle with unprecedented level of accuracy, verifying the Local Position Invariance by means of frequency measurements probing the varying flow of time experienced by the spacecraft H-maser during its highly eccentric orbit. The relevance of this experiment within the framework of relativity comes from the modern physics need of understanding and trying to unify the two cornerstones of Quantum Mechanics and General Relativity, which are not compatible. The most accurate measurement of the EEP violation parameter performed so far has been recently carried out with the Galileo satellites 5 and 6 (GSAT0201 and GSAT0202), reaching an accuracy of $\delta\varepsilon \approx 3 \times 10^{-5}$, improving the previous Gravity Probe A result by more than a factor 4. The current RadioAstron Gravitational Redshift experiment aims to improve the Gravity Probe A result as well by an order of magnitude, reaching $\delta\varepsilon \approx 10^{-5}$.

The RadioAstron SPEKTR-R is a Russian space radio telescope, launched on July 18 2011 from the Baikonour Cosmodrome in Kazakhstan. Its main purpose is to operate in the field of space VLBI science. However, its ultra stable H-maser, combined with the highly eccentric orbit of the spacecraft, have made it perfectly suitable for the realization of gravitational redshift experiments.

The experiment presents several challenges, both related to technical difficulties such as hardware synchronization modes of the satellite radio system, and to the uncertainties involved in the actual frequency measurements. The inaccurate knowledge of the spacecraft state vector, the impossibility to measure the frequency offset between ground and space H-masers without making use of the EEP principle redshift formula, the noise affecting the observations and the uncertainty in the coordinates of the main tracking station (Pushchino) are the most relevant issues.

In support of the RadioAstron team, a simulation study was carried out to investigate the statistical properties of the EEP violation parameter estimation process with the purpose of understanding and describing the limiting factors in the experiment. A covariance analysis by means of a multi-arc least squares orbit determination estimation including ε in the list of estimated parameters, has been done using the Tudat software and using real orbital data corresponding to the experiments time intervals as a reference for the algorithm initial step. Under the assumptions of statistically independent arcs, white Gaussian noise, arc-wise constant frequency offsets for every station in one way observables, the simulation of RA Doppler measurements within the orbit determination process has shown that the experiment accuracy mainly depends on the observations noise and the a priori knowledge of the H-masers offset uncertainty. The spacecraft state vector parameters, as well as the Pushchino station coordinates, are not correlated to ε, whose correlations with one way frequency biases are, on the other hand, not negligible. Given a fractional frequency noise of 10^{-12} and an Allan deviation reference value of 10^{-13} for one hour averaging time, the resulting EEP violation parameter accuracy, according to the simulations study, corresponds to an order of magnitude of 1.9608×10^{-5} and the mean value of the correlations of ε with the one way frequency offsets is right above 0.5.

The main assumption of white Gaussian noise is supported by the analysis of real frequency data from the spacecraft with PRIDE tracking algorithms. However, results are still considered quite optimistic because of the very simple radiation pressure force model adopted (cannonball), two way observations been considered completely unbiased and other possible unmodelled noise effects neglected. Moreover, the assumption of constant offsets during one hour observation times is not completely realistic since it is known that they experience a drift, even though this is believed to be extremely small in one hour time.

The simulations study also shows that ε and Δf_0 could be decorrelated in particular circumstances of low noise and a favourable geometry of the spacecraft trajectory at the times of the Doppler observations but this aspect is still under investigation.

Chapter 1

Introduction

This thesis is intended to provide support to the RadioAstron Gravitational Redshift Experiment by means of a study of the achievable experiment accuracy based on the current capabilities and the data collected through the several Doppler tracking sessions performed with the Russian satellite. The results presented throughout the report have been achieved through simulations carried out with the TUDelft Astrodynamics Tool Software (Tudat). The experiment topic involves several different fields of study which are all intimately connected and will be introduced in the following sections.

After giving some background information related to the fundamental physics aspect, the RadioAstron mission and satellite characteristics in sections 1.1 and 1.2, the experiment is described in 1.3. Past and future gravitational redshift tests are reported in 1.4 and 1.5. Finally, the research questions formulated for the thesis project are given in 1.6.

1.1 Background information

General Relativity and Quantum Mechanics are the two cornerstones of modern physics. However, they are very distinct theories and are not compatible. New attempts for their unification imply tiny violations of General Relativity. More specifically, the new developed theories predict a violation of the Einstein Equivalence Principle ([4]), therefore several tests have been going on. Gravitational Redshift experiments are fundamental in this framework since their purpose is to verify the Local Position Invariance: one of the three principles into which the EEP can be split. So far the best ever achieved accuracy has been recently obtained with the 'GREAT' experiment, conducted with two European GNSS Galileo satellites ([8] and [9]) who has improved by more than a factor of 4 the previous old Gravity Probe A experiment result. The RadioAstron Gravitational Redshift Experiment follows this path aiming to reach an accuracy similar to the 'GREAT' experiment. Future experiments are introduced in section 1.5.

RadioAstron Spektr-R is a Russian space radio telescope which was launched in a highly elliptical orbit on July 18 2011 from the Baikonour Cosmodrome. This satellite is designed for operating space VLBI science increasing the resolution obtained by ground VLBI. The possibility of using a 10 m space radio telescope has brought very significant improvements in the angular resolutions of radio astronomical observations ([10]). The main ground radio data acquisition station is Pushchino, located near Moscow. The orbit of RadioAstron is perturbed by the Moon in such a way that the radio telescope can be adopted for different kinds of VLBI observations of different sky regions during its mission lifetime ([10]). Its main scientific goal is related to purely astrophysical studies, regarding for instance objects like black holes, active galactic nuclei (AGN) and interplanetary and interstellar plasma ([1]). However, thanks to the H-maser which is onboard the satellite, it has been possible to perform a gravitational redshift test taking advantage of the highly elliptic orbit of the spacecraft. Further details of the experiment are given in 1.3.

1.2 RadioAstron Spektr-R Spacecraft

The Spektr-R spacecraft carries a Space Radio Telescope made up of a 10 m diameter antenna which is equipped with 1.35, 6.2, 18 and 92 cm receivers ([1]). An overview of the SRT is shown here:
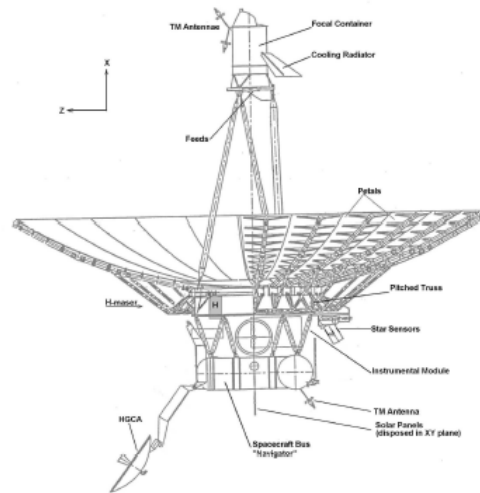
Figure 1.1: *SRT configuration. Taken from [1]*

As seen from Figure 1.1, on the other side of the satellite there is also a communication antenna which is used to transmit the data acquired by the SRT. The power is generated through solar panels which are in the $x - y$ plane and, concerning the attitude determination, the satellite is equipped with star sensors used for precise attitude control and radio telescope pointing.

The science equipment onboard RadioAstron is pictured in Figure 1.2:
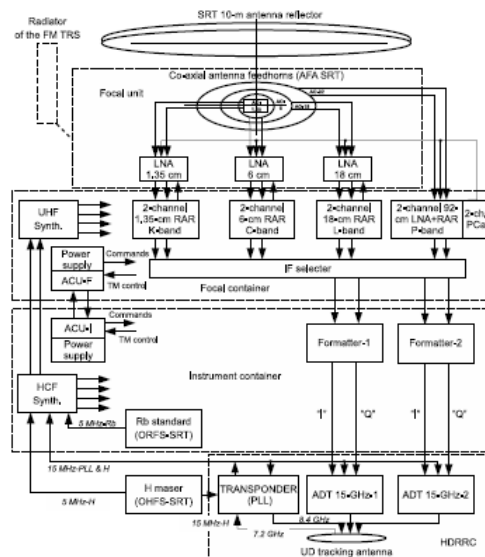
Figure 1.2: *Science complex picture from [1]*

The main components of the science complex, according to [1] are characterized by the

- Blocks of co-axial antenna feeds
- LNA blocks
- Radio-astronomy receivers
- Frequency standards blocks: two Hydrogen masers and two rubidium frequency standards

The characteristics of the Hydrogen maser frequency standard can be found here below, according to [6]:

Table 1.1: *H-maser characteristics as reported in [6]. $\sigma_y(\tau)$ represents the Allan deviation corresponding to an averaging time τ.*

$\sigma_y(\tau = 1000s)$	3×10^{-15}
$\sigma_y(\tau = 1h)$	2×10^{-15}
Drift (1 day)	1×10^{-15}
Drift(1 year)	2×10^{-13}

The onboard hydrogen frequency standard provides a reference signal of 5 MHz or 15 MHz, while the rubidium frequency standard is 5 MHz ([1]). Another reference signal used for RadioAstron is the 15 MHz signal of the phase synchronization loop of the HDRRC that is synchronized thanks to the signal from an H-maser of a ground tracking station. The data acquired by the SRT is sent to the ground station through the HDRRC complex which works with several synchronization modes described later on.

The spacecraft is also equipped with an array of retroreflectors for laser ranging purposes. In particular there are 100 angle retro-reflectors FA674M as reported in [2]. The configuration of the laser ranging equipment is illustrated in the following figures:
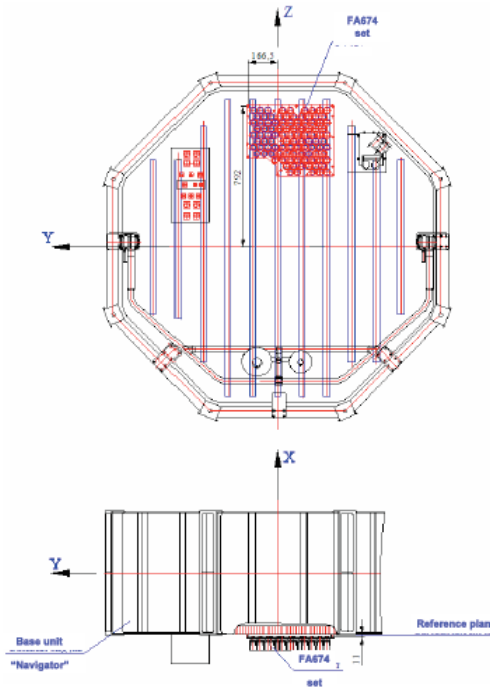
Figure 1.3: *Layout of laser retroreflector array. Picture from [2].*
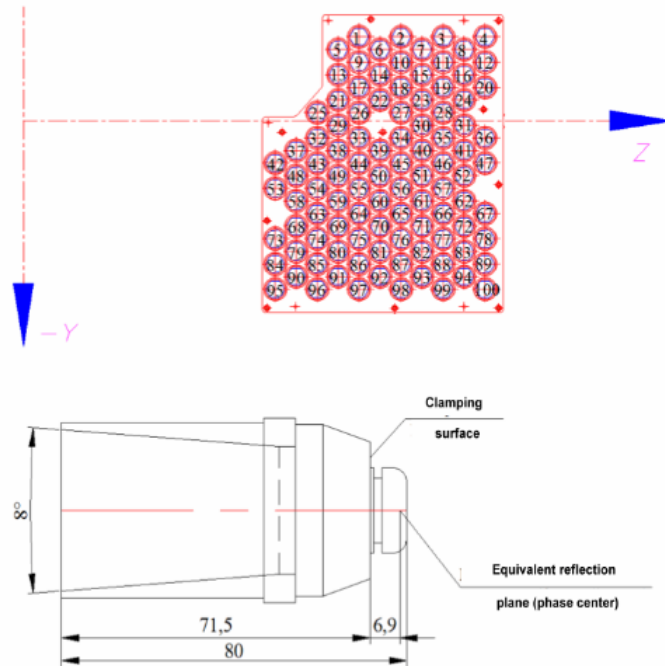
Figure 1.4: *Array numeration and general configuration. Picture from [2].*

After the launch the spacecraft was inserted into a highly elliptical orbit characterized by a 578 km perigee and 333500 km apogee, with an orbital period of 8.32 days ([1]). Since the mission lifetime would have been too short (too low perigee height) two orbit corrections with thrusters were made on March 12012, extending the mission lifetime to about 9 years. RadioAstron's orbit is strongly perturbed by the Sun and the Moon and it is predicted that its orbit eccentricity will change from 0.96 to 0.59 during its lifetime and the inclination will vary in the interval 10 - 85 deg. ([1]). The radius of perigee varies from 7000 km to 81500 km, while the radius of apogee from 280000 to 353000 km. The evolution of the orbit in time is given in the next group of figures:
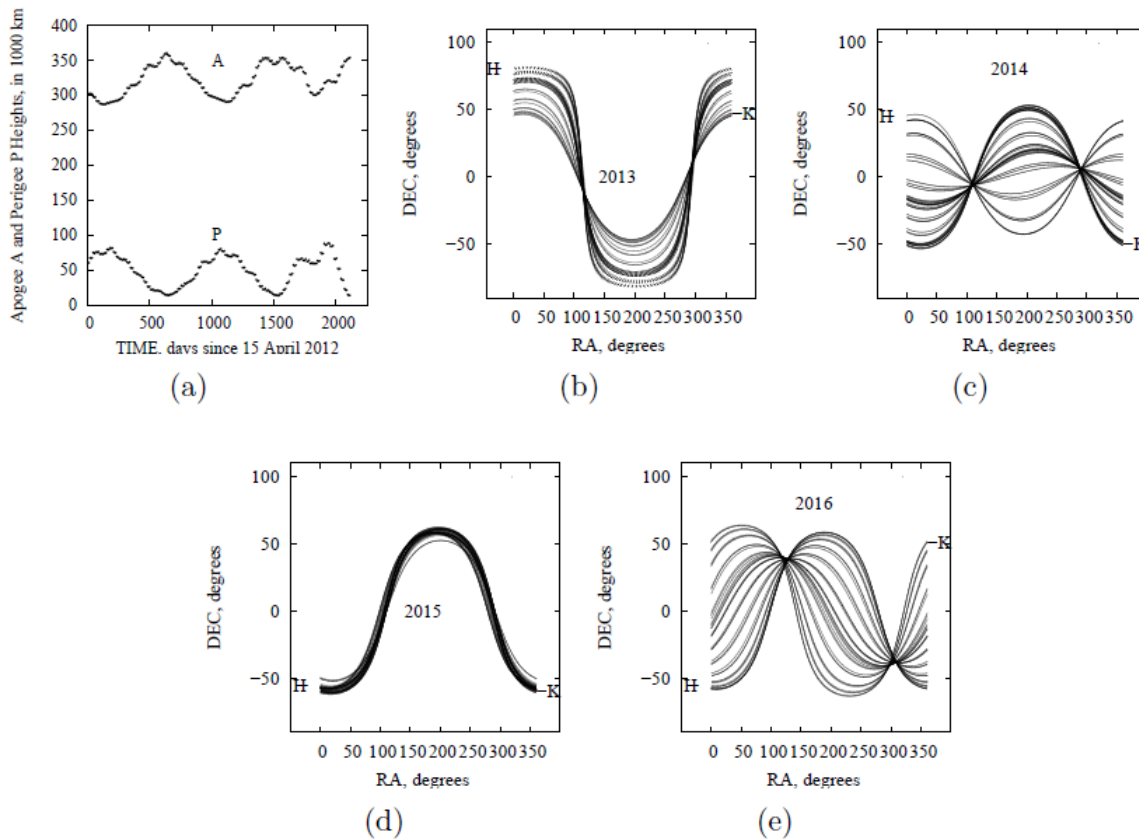
Figure 1.5: *Perigee and Apogee heights (a), Declination and Right Ascension evolution through the years as reported on [1](b,c,d,e)*

A very important source of perturbation for RadioAstron is the solar radiation pressure. Due to the shape of the satellite, the radiation pressure acts on different elements of the SRT in different ways and at different times of the orbit; therefore the effect is significant. Moreover, due to the same effect, a torque acts on the satellite and thus a set of reaction wheels constantly works in order to keep the attitude fixed. Since the torque produces an effect which increases over time, the reaction wheels need to increase their rotational speed as well in order to balance the perturbation. To accomplish this, the reaction wheels need to be unloaded in turn and this produces other perturbations to the spacecraft center of mass ([1]).

The orbital parameters, as measured on April 142012, are given here:

Table 1.2: *Orbital elements of RadioAstron on April 142012, as reported on [1]*

Major axis	$a = 174714.234km$
Eccentricity	$e = 0.692$
Orbital inclination	$i = 79.69deg$
Ascending node longitude	$W = 300.55deg$
Argument of perigee	$w = 303deg$
Time of perigee passage	$07:12:37.00$ UTC 14 April 2012
Orbital period	$\approx 8.5d$

Given the challenging aspects of RA orbit determination, the OD for the RadioAstron mission support has been carried out by estimating additional parameters related to solar radiation pressure and the perturbing accelerations due to the unloading of the reaction wheels. The details of this approach are found in [11]. The orbital data of the satellite are found in [12].

1.3 RadioAstron gravitational redshift experiment

The special equipment onboard RadioAstron, in particular the presence of a high performance Hydrogen maser (H-maser) is extremely interesting for the performance of a gravitational redshift test. Comparing the frequency of the space borne H maser with a same frequency standard located on Earth (at Pushchino station), can lead to a better accuracy than the previous tests performed so far, described in section 1.4 ([6]).

The purpose of the experiment is to verify the following equation, derived in chapter 2, section 2.6, following the approach of [13]:

$$\frac{\Delta f_{grav}}{f} = \frac{\Delta U}{c^2} \tag{1.1}$$

This is the first order approximation in $1/c^2$ of the gravitational redshift effect.

Since the gravitational redshift is a direct measure of the validity of Einstein's Equivalence Principle, any violation of this effect (in the way predicted by Equation 1.1) would mean that the EEP, as described in section 2.2, does not hold. The deviation from Equation 1.1 can be expressed, according to [4], as:

$$\frac{\Delta f_{grav}}{f} = \frac{\Delta U}{c^2}(1 + \varepsilon) \tag{1.2}$$

where ε represents the violation parameter (the quantity measured through the gravitational redshift experiments), being equal to 0 in General Relativity.

The main concept is to compare the frequencies of the Ground H-Maser (GHM) and the Space H-maser (SHM) to probe the varying flow of time. This is done by means of radio links between the ground stations and the spacecraft. According to [6], the frequency shift experienced by a signal sent from the spacecraft to the ground is:

$$f_s^{\downarrow} = f_s + \Delta f_{grav} + \Delta f_{kin} + \Delta f_{instr} + \Delta f_{media} \tag{1.3}$$

where $f_s^{\downarrow}$ is the signal's frequency as received on the ground, f_s is the frequency sent from the spacecraft, Δf_{grav} is the gravitational redshift effect (actually in the case of a one way space to ground link it is a blueshift), Δf_{kin} is the kinematic contribution due to the relative velocity between the station and the satellite, Δf_{media} is the perturbing effect of troposphere and ionosphere and finally Δf_{instr} is related to the instrumentation noise.

In the case of RadioAstron the main difficulty is that it is not possible to have a direct measure of f_s and thus this quantity is expressed as ([6]):

$$f_s = f_e + \Delta f_0 \tag{1.4}$$

where f_e is the frequency of the GHM and Δf_0 is an offset which is a function of time. The different environmental conditions, in fact, determine a slight shift between the two frequency standards. The cavity "pulling" effect, in particular, may produce a drift of the bias over long times ([14]). Moreover, the accurate determination of Δf_0 is not possible without making use of Equation 1.2. This problem is solved by measuring the difference in gravitational redshift rather than its absolute value ([4]).

In principle, the accuracy of the experiment is given by the differentiation of Equation 1.2 ([6]):

$$\delta\varepsilon = \frac{\delta\frac{\Delta f_{grav}}{f}}{\frac{\Delta U}{c^2}} - \frac{\frac{\Delta f_{grav}}{f}}{\frac{\Delta U}{c^2}^2}\delta\frac{\Delta U}{c^2} \tag{1.5}$$

which can be approximated as:

$$\delta\varepsilon \approx \frac{\delta\frac{\Delta f_{grav}}{f} - \delta\frac{\Delta U}{c^2}}{\frac{\Delta U}{c^2}} \tag{1.6}$$

by making use of Equation 1.2 with $\varepsilon = 0$.

It is clear then that the accuracy of ε depends obviously on the errors in both the gravitational redshift measurement and the gravitational potential computation. They are indeed intimately connected because they are functions of the spacecraft state vector uncertainty, but the former also of the several noise sources appearing in Equation 1.3, among which the clock bias is the most difficult to estimate. The statistical properties of this offset, together with the characteristics of the observations noise and the spacecraft precise orbit determination, represent, in fact, the key aspects influencing the experiment accuracy. Understanding how these factors relate to each other and coming up with a realistic error budget is the objective of this thesis work and is extensively described throughout chapters 4 and 5.

The aim of the RadioAstron gravitational redshift experiment is to reach an accuracy of $\delta\varepsilon \approx 10^{-5}$. The contribution to the gravitational redshift due to the Moon can be neglected in the computations so only the Earth's gravitational field is considered.

1.4 Past experiments

The most relevant past experiments that were carried out to measure the gravtational redshift, are the Pound and Rebka, the Gravity Probe A and the most recent "GREAT" experiment performed with the Galileo satellites.

1.4.1 Pound and Rebka

The experiment was performed in 1960 using the 22.5 m tower of the Jefferson Physical Laboratory at Harvard University. The signals adopted were the gamma rays coming from Fe^{57} decay. These signals were emitted from the top of the tower and received on the ground by another Fe^{57} nucleus. When gamma rays reached the bottom of the tower they were blueshifted: their frequency in fact became larger according to the relativistic effect, this meaning that the absorption of the signal from the ground Fe nucleus was less efficient. The gravitational redshift effect was computed by moving the electromagnetic wave source at the top of the tower in order to produce a Doppler shift that would compensate the effect of gravity. The gamma ray energy was 14.4 keV and the velocity of the top source that determined the maximum absorption of the energy at ground was considered a measure of the frequency shift. The frequency shift, according to Equation 2.26 would be $gh/c^2 \approx 10^{-15}$ for $h = 22.5m$ and the accuracy achieved with the experiment was 1 % ([13], [15]).

1.4.2 GP-A

Gravity Probe A was a spaceborne experiment realized in 1976 by means of a rocket carrying onboard a Hydrogen maser clock and reaching an altitude of 10^4 km. Through frequency measurements of the signals emitted by the probe and with a very smart design of the compensation scheme it was possible to distinguish the gravitational redshift effect with an accuracy of 1.4×10^-4 ([3]). Here the scheme of the measurements is reported:
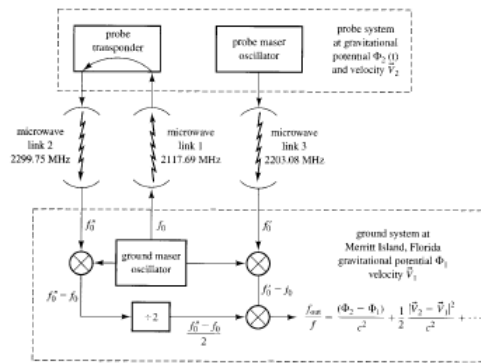
Figure 1.6: *GP-A experiment diagram, as reported in [3].*

As seen from Figure 1.6 the two way probe tracking is very useful since it enables to compensate the gravitational effect providing a detailed measure of the first order Doppler shift (relativistic Doppler shift). Therefore, once obtained a measure of the first order shift, it is subtracted by the difference between the spaceborne and ground H-maser frequencies in order to calculate the second order Doppler shift which is exactly the gravitational redshift effect.

A very similar approach is adopted in the RadioAstron gravitational redshift experiment. However the substantial difference between the two experiments is that RadioAstron is not designed for the gravitational redshift experiment and thus it is more complicated to get the oscillating rate of the onboard H-maser.

1.4.3 GREAT project

The Galileo satellites 5 and 6 (GSAT0201 and GSAT0202), which were inserted in the wrong orbits due to an error during launch (August 30th 2014), have been used to carry out a gravitational redshift experiment reaching an accuracy of 3×10^-5 on the EEP violation parameter (as reported in [8] and [9]). The two satellites were, in fact, inserted in elliptic orbits and, being both equipped with H-masers, this has made them two perfect candidates to test the Local Position Invariance. The acronym "GREAT" stands for Gravitational Redshift experiment with Eccentric sATellites.

Both the teams who have analysed the Galileo satellites data have adopted a least squares algorithm to fit the measurements estimating both ε and a bias, the latter being assumed as a linear function of time ([8]). The satellites state vector parameters were not estimated but some SLR data was acquired in order to improve their orbital knowledge ([9]).

The estimation approach adopted by the Galileo teams is similar to the one used for the simulation of the RadioAstron gravitational redshift experiment in this project study. The main difference is that the simulations described in chapter 4 were set up with a much larger number of estimated parameters, including also the satellite state vector and the radiation pressure coefficient.

1.5 Future experiments

A future experiment that will test the local position invariance is the ACES mission which is in preparation. This ESA mission is designed to test the EEP by placing a very precise atomic clock onboard the ISS and compare its frequency with ground based clocks through both radio and optical links. The achievable level of the gravitational redshift measurement is claimed to be 3×10^{-6}, according to [16]. Since the ISS orbit is almost circular the stability of the clock needs to be extremely high for performing this test.

1.6 Research questions

After introducing the experiment and its several challenging aspects, the following research questions are defined and answered throughout the thesis report:

- What is the influence of the satellite state vector uncertainty on the EEP violation parameter estimation?
- What is the impact of the Pushchino tracking station position uncertainty on the experiment?
- How can both dynamical and observation models for the gravitational redshift experiment be simulated?
- What are the limiting factors in the experiment?
- How does the observations noise affect $\delta\varepsilon$ and its correlations?
- What is the influence of the clock offset a priori uncertainty on the experiment accuracy?
- Which conclusions can be drawn about the achievable experiment accuracy?

Chapter 2

Fundamental physics of the project study

This chapter provides the fundamental theory involved in the RadioAstron Gravitational Redshift Experiment and the simulations study. It is the theory of General Relativity formulated by Einstein. Particular focus will be given to the Equivalence Principle which is the cornerstone of the whole theory of General Relativity. It is based on the concept that gravity is not a force but a metric theory. In other words, the trajectories of objects follow straight lines in the curved spacetime which is shaped by the masses. Starting from an introduction to the special relativity, given in 2.1, the EEP and the GR are presented in sections 2.2 and 2.3 up to the level required for defining and understanding the Gravitational Redshift. This is treated in the separate section 2.6. The main reference used for the description of the fundamental physics given in this chapter is [13].

2.1 Introduction to Special Relativity

The main assumption behind Einstein's special theory of relativity was that the speed of light in vacuum is a constant in every reference frame (actually in 1887 the Michelson-Moorley experiment had already confirmed this, setting the basis for developing further studies about Newtonian mechanics or Maxwell equations). This assumption is fundamental to understand the concept of flat spacetime.

In special relativity each inertial reference frame is still defined according to the first Newton law and is therefore characterized by a notion of time according to which the second derivatives of the spacial coordinates respect to time of a free particle (a particle on which no forces act) are equal to zero. However, the Newtonian principle of addition of velocities (which comes from the Galilean transformations defined in classical mechanics to describe relations between two different inertial frames) does not agree with the main assumption made about the velocity of light. According to the Galilean transformations, in fact, light should have different velocities in different inertial frames, based on the relative velocity existing between the frames. This problem is solved in special relativity by admitting that the notion of time and simultaneity of events is different for each inertial reference frame. Each inertial frame is then characterized by a set of 4 coordinates (t, x, y, z) forming the four dimensional flat spacetime. A point defined in the spacetime is called an event in order to underline that it is related to a certain position and a certain time. The geometry of the flat spacetime is non Euclidean; therefore a new definition of distance needs to be introduced. The length of the infinitesimal line element in flat spacetime is defined as:

$$ds^2 = -(cdt)^2 + (dx)^2 + (dy)^2 + (dz)^2 \tag{2.1}$$

where s is the length, t is the coordinate time and x, y ad z are the spacial coordinates. Equation 2.1 is invariant for every system of coordinates defined in flat spacetime. It enables to calculate the distance between points in spacetime.

Defining the tensor:

$$\eta_{\alpha\beta} = \begin{pmatrix} -1 & 0 & 0 & 0 \\ 0 & 1 & 0 & 0 \\ 0 & 0 & 1 & 0 \\ 0 & 0 & 0 & 1 \end{pmatrix} \tag{2.2}$$

the differential of the line element can then be expressed in the more compact form:

$$ds^2 = \eta_{\alpha\beta} dx^\alpha dx^\beta \tag{2.3}$$

According to the notation adopted, the repeated indices imply a summation extended to the four coordinates. This is the Einstein summation convention. $\eta_{\alpha\beta}$ is the metric of the flat spacetime, which is also known under the name of Minkowski spacetime, from the mathematician who provided its mathematical model.

According to the definition of the line element, when computing the distance between two points in the spacetime, it is possible to distinguish 3 different cases:

- $(\Delta s)^2 > 0$
- $(\Delta s)^2 = 0$
- $(\Delta s)^2 < 0$

When $(\Delta s)^2 > 0$ the two points are said to be spacelike separated, when $(\Delta s)^2 = 0$ they are null separated or light separated, and when $(\Delta s)^2 < 0$ they are timelike separated. Two spacelike separated points are, for instance, points that are in two different spacial positions at the same time ($\Delta T = 0$). Two light separated points are points for which for example $\Delta x = c\Delta T$ and $\Delta y = \Delta z = 0$; and two timelike separated points are for instance points that are in the same position but at different times.

These definitions allow one to define the so called light cone of a generic point P in the flat spacetime: it is the locus of points that are light (or null) separated from P. To each point P in spacetime a light cone is associated: one can say that the upper part of the light cone is the locus of points generated by a light pulse emitted from P, while the lower part by a light pulse converging in P.

Calling "world line" a generic trajectory in the spacetime, from the light cone definition given earlier it follows that particles with a non zero rest mass always follow timelike world lines: the cone is in fact delimited by world lines followed by light and thus particles which move along world lines that lie inside the light cone travel at velocities that are always smaller than light speed.

Given these basic definitions, a clock is defined as a device that can measure distances along timelike world lines and a ruler as a device able to measure distances along spacelike world lines.

A very important quantity which can be introduced is the so called proper time, τ, defined by the following relation :

$$d\tau^2 = -\frac{ds^2}{c^2} \tag{2.4}$$

Equation 2.4 defines a quantity which is measured in real numbers and has the dimension of time. It represents the time that a clock would measure along a particle's world line.

A first relativistic effect can be immediately derived starting from the definition of the proper time. The proper time between two points A and B that are timelike separated can be in fact computed by integrating Equation 2.4 and applying the definition of ds given in Equation 2.1, obtaining:

$$\tau_{AB} = \int_A^B d\tau = \int_A^B dt\sqrt{1 - \frac{v^2}{c^2}} \tag{2.5}$$

with t being the coordinate time, therefore:

$$d\tau = dt\sqrt{1 - \frac{v^2}{c^2}} \tag{2.6}$$

This relation explains the phenomenon of time dilation: time measured by an observer with a velocity v is shorter than the difference between the time coordinates at the two timelike separated points. Equation 2.6 describes how to measure this time difference.

2.2 Einstein's Equivalence Principle

The main reference of this section is [13], chapter 6.

In the previous section introducing the special relativistic mechanics, the parameter m representing the mass of a particle is the inertial mass as defined by Newton's second law. However, Newton's theory of gravity defines another concept of mass, called gravitational mass. This is defined by the relation expressing the gravitational attraction force between two bodies:

$$F_{12} = \frac{Gm_1 m_2}{|\vec{r_2} - \vec{r_1}|^2} \tag{2.7}$$

where m_1 and m_2 are the gravitational masses, G is Newton gravitational constant and $\vec{r_2}$ and $\vec{r_1}$ are the position vectors of body 1 and 2 defined in an inertial frame.

The concepts of inertial and gravitational masses are therefore different: the first is related to the inertial properties of the body while the second is a measure of the strength of the body's gravitational field, as seen in Equation 2.7. In particular the inertial mass is a concept which is not related to a specific force and thus does not depend on the origin of the force; gravitational mass instead is strongly related to the gravity force. In principle there is no particular reason why these two different mass concepts should be exactly equal. What actually can be said is that inertial and gravitational masses must be indeed proportional since all experiments confirm that all bodies fall with the same acceleration in a gravitational field. However, the equality of gravitational and inertial mass is today an experimental fact. This equality has been tested many times through several experiments; it is actually one of the most accurately tested principles in physics. (e.g. torsion pendulum experiment conducted in 1994 [17]).

The idea of equivalence between gravitational and inertial mass brings the conclusion that it is in principle not possible to distinguish the effect of a gravitational field from the effect of a uniform acceleration. Einstein's Equivalence Principle (EEP) expresses exactly this concept and is the fundamental principle that sets the basis for the theory of General relativity. It is hereby given:

" Experiments in a sufficiently small freely falling laboratory, over a sufficiently short time, give results that are indistinguishable from those of the same experiments in an inertial frame in empty space."

According to Einstein, since it is not possible to distinguish the effect of a uniform gravitational field respect to the effect of a uniform acceleration, the equality between gravitational and inertial mass must hold. If gravity had a different effect on masses of different composition then the EEP principle would not hold. It is exactly this equality that represents the basis for Einstein's geometric theory of gravity: if all bodies fall with the same acceleration independently of their composition it can be said that the curve followed by them is a property of the spacetime and not really the consequence of a force. This inspired Einstein in developing the concept that Newtonian gravity is not really a force but consists of a geometric property of the spacetime. In other words objects that are affected by gravitational fields follow 'straight' trajectories in a curved spacetime.

The Einstein Equivalence Principle can be better clarified if split into its different aspects. A good distinction between the main relevant statements included in the principle is provided by [18]:

- Free fall under gravity is the same for all substances (this is known as the Weak Equivalence Principle)
- For freely falling observers special relativity applies locally (this principle is known as the Local Lorentz Invariance)
- The preceeding properties apply at all times and places (this is known as the Local Position Invariance)

The measurement of the Gravitational Redshift effect, which will be treated in section 2.6, is a way of testing in particular the Local Position Invariance of the EEP.

2.3 Introduction to General Relativity

The final generalization of the theory of relativity is a theory which is consistent with the special relativity principles and provides a new way of explaining Newtonian gravity as a geometric property of the spacetime. The main principle is that mass determines a curvature in the spacetime.

The curved spacetime is not characterized by the Minkowski metric shown in section 2.1 but more in general, by a metric which can be described as follows:

$$ds = g_{\alpha\beta} dx^\alpha dx^\beta \tag{2.8}$$

where $g_{\alpha\beta}$ is a symmetric tensor depending on position and coordinate time.

At this point the Equivalence Principle plays a fundamental role: it suggests that the properties of the curved spacetime in a local region around a point P, are indistinguishable from the properties of flat spacetime.

Mathematically speaking this turns into the assumption that in a point P of curved spacetime it is always possible to choose a system of coordinates such that:

$$g'_{\alpha\beta}(x'_P) = \eta_{\alpha\beta} \tag{2.9}$$

and:

$$\frac{\partial g'_{\alpha\beta}(x'_P)}{\partial x'^\gamma} = 0 \tag{2.10}$$

where $\eta_{\alpha\beta}$ is the Minkowskian metric.

A coordinate system defined by these conditions is then called a "local inertial reference frame" since it has the same properties of an inertial frame of flat spacetime.

This assumption drives also the concept of vectors in the curved spacetime: here a vector is defined in a certain point of curved spacetime where it obeys to the flat spacetime rules. At every point in curved spacetime vectors can be then defined in the 'tangent spacetime'. Therefore a vector is defined as follows:

$$\boldsymbol{a}(x) = a^\alpha(x)\hat{\boldsymbol{e}}_\alpha(x) \tag{2.11}$$

and the idea of the scalar product is the same as in flat spacetime. It is important to underline that in Equation 2.11 every term is a function of the position x: in particular, the orthonormal vector basis differs form point to point in the spacetime defining a tangent spacetime according to the geometry of the curvature. This is the difference with respect to the flat spacetime.

Of particular interest are orthonormal bases, defined by:

$$\boldsymbol{e}_{\hat{\alpha}} \cdot \boldsymbol{e}_{\hat{\beta}} = \boldsymbol{\eta}_{\hat{\alpha}\hat{\beta}} \tag{2.12}$$

2.4 General form of Equations of Motion in curved spacetime

The main reference for this subsection is [13], chapter 8.

In flat spacetime the equation of motion of a non zero rest mass particle reduces to the condition imposed by Newton's first law. However, a test particle moving in a general curved spacetime with metric $g_{\alpha\beta}$, has a different equation of motion. Timelike world lines followed by free particles in curved spacetime are called "geodesics" and, according to Einstein, the general equation of motion is described by:

$$\frac{d^2x^\alpha}{d\tau^2} = -\Gamma^\alpha_{\beta\gamma}\frac{dx^\beta}{d\tau}\frac{dx^\gamma}{d\tau} \tag{2.13}$$

where $\Gamma^\alpha_{\beta\gamma}$ represent the "Christoffel symbols" which are defined by:

$$g_{\alpha\delta}\Gamma^\delta_{\beta\gamma} = \frac{1}{2}\left(\frac{\partial g_{\alpha\beta}}{dx^\gamma} + \frac{\partial g_{\alpha\gamma}}{dx^\beta} - \frac{\partial g_{\beta\gamma}}{dx^\alpha}\right) \tag{2.14}$$

In Equation 2.13 x^α still represents the four vector coordinates according to the four vector definition provided in the special relativistic mechanics, but in this case the equation of motion is described in the most general form for a test particle moving along a timelike worldline in a curved spacetime. The Christoffel symbols are intimately related to the spacetime metric and its derivatives: they represent the influence that the curved spacetime has on the particles motion.

Concerning the motion of light rays (zero rest mass particles) it is necessary to introduce a new parameter in order to express the equations of motion since the spacetime distance for light rays is always zero. Therefore, also in the general case, it is possible to choose a parameter γ such that Equation 2.13 holds with respect to γ and not τ.

2.5 Observable effects of EEP

Based on what is explained in section 2.2, every experiment that confirms the equivalence between gravitational and inertial mass can be seen as an observable effect of the EEP. As previously said, this equality has been tested with great accuracy in physics. The first very important experiments were performed with torsion pendulums, for instance the experiment of the torsion balance performed by Eotvos. It consisted in using two masses placed on the opposite ends of a rod which was hung from a thin fiber. On the rod there was a mirror reflecting light beams to a telescope. If there was a rotation of the rod, this would have been detected with very high accuracy through the telescope. The forces acting on the system were the fiber tension, the gravitational force and the inertial centrifugal force which would have balanced the system. The experiment was performed with masses of

different compositions to test if the forces acting on them would be different. If so, there would be a torsion.

The greatest observable effects of the EEP were then obtained using the Solar System as a laboratory. In particular, through the lunar laser ranging experiments performed so far, by measuring very accurately the relative motion between the Earth and the Moon it was observed that the accelerations of the Earth and the Moon about the Sun were the same. Since the Earth and Moon have very different compositions this is a great confirmation that the EEP is not violated. More precise analyses have been recently studied in order to improve the accuracy of the strong equivalence principle tests with Lunar Laser ranging (LLR). An overview of the challenges involved with this kind of experiments is provided in [19] where the data modeling is treated.

Among the observable effects of the EEP, the gravitational redshift is one of the most relevant effects which can be observed with a high level of accuracy.

2.6 Gravitational redshift

The main reference for this subsection is [13], chapter 9.

The gravitational redshift is a frequency shift effect due to the spacetime curvature which affects electromagnetic signals that travel through a region in which the gravitational potential is not uniform.

Given two observers that are located in different points characterized by different gravitational potentials, the rates of emissions of signals are observed in a different ways by the two observers. Considering for instance the case of a body of radius R, if f indicates the signal frequency, the following relation holds up to the first order approximation:

$$f_\infty = \left(1 - \frac{GM}{Rc^2}\right) f_*$$ (2.15)

where f_∞ is the frequency observed far away from the star (where the potential is assumed to be zero) and ω_* is the frequency observed at the surface of the star.

To prove Equation 2.15, a solution to Einstein's equation for curved spacetime is needed. This is the Schwarzschild solution which exactly describes the geometry of the curved spacetime affected by a homogeneous spherical body. The Schwarzschild metric is described by the differential line element expressed in spherical coordinates:

$$ds^2 = -\left(1 - 2\frac{GM}{c^2 r}\right)(cdt)^2 + \left(1 - \frac{2GM}{c^2 r}\right)^{-1} dr^2 + r^2(d\theta^2 + sin^2\theta d\phi^2)$$ (2.16)

which is time independent and spherically symmetric. G is the Gravitational constant and M the total mass of the spherical object.

Given the formula for the energy of a photon measured by an observer with four velocity $\boldsymbol{u}_{obs}$:

$$E = hf = -\boldsymbol{p} \cdot \boldsymbol{u}_{obs}$$ (2.17)

and considering the time independence of the metric in Equation 2.16 , a rigorous derivation of the gravitational redshift can be achieved.

Given that for a static observer at radius r the spatial components of the four velocity are zero and only the time component exists, this component can be computed starting from the normalization equation:

$$\boldsymbol{u}_{obs}(r) \cdot \boldsymbol{u}_{obs}(r) = g_{\alpha,\beta} u^\alpha_{obs}(r) u^\beta_{obs}(r) = -1 = g_{tt}(r)(u^t_{obs}(r))^2$$ (2.18)

and thus

$$u^t_{obs} = \left(1 - \frac{2GM}{c^2 r}\right)^{-1/2}$$ (2.19)

This means that the time component of $\boldsymbol{u}_obs$ can be expressed in terms of the so called "Killing vector" associated with the time independence of the metric:

$$u^t_{obs}(r) = \left(1 - \frac{2GM}{c^2 r}\right)^{-1/2} \xi^\alpha$$ (2.20)

with

$$\xi = (1, 0, 0, 0)$$ (2.21)

being the killing vector. In general a killing vector is a vector that defines a direction along which the metric is symmetric, in this case it is the time direction.

Computing the energy of the photon at the two different locations, it is obtained:

$$hf_* = \left(1 - \frac{2GM}{R}\right)^{-1/2} (-\boldsymbol{\xi} \cdot \boldsymbol{p})_R \tag{2.22}$$

and

$$hf_\infty = (-\boldsymbol{\xi} \cdot \boldsymbol{p})_\infty \tag{2.23}$$

but since $-\boldsymbol{\xi} \cdot \boldsymbol{p}$ is always conserved due to the time symmetry of the metric, the relation between the two observed frequencies is:

$$f_\infty = f_* \left(1 - \frac{2GM}{c^2 R}\right)^{1/2} \tag{2.24}$$

This relation if approximated to the first order in $1/c^2$, leads to the more familiar equation:

$$f_\infty = f_* \left(1 - \frac{GM}{c^2 R}\right) \tag{2.25}$$

where one can distinguish the Gravitational potential difference between R and infinity as GM/R. Therefore, the frequency shift experienced by the photons can be expressed with good approximation by:

$$\frac{\Delta f}{f_0} = \frac{\Delta U}{c^2} \tag{2.26}$$

where ΔU is the difference gravitational potential difference between the two observers.

Chapter 3

Methodological foundation of the experiment

In this chapter the theoretical aspects concerning the methods and principles on which the RadioAstron gravitational redshift experiment is based are described. The Doppler tracking physics is explained in section 3.1 where the detailed model of the frequency transfer is provided, followed by an overview of the noise sources. The orbit modeling and determination are treated in sections 3.2 and 3.3 where particular attention is given to the explanation of the least squares method. This is, in fact, the mathematical and statistical tool adopted in the simulations of the gravitational redshift experiment.

3.1 Doppler tracking

The purpose of Doppler tracking is to measure the relative velocity between a station on Earth and the spacecraft by means of radio links that enable to compare observed frequencies with ground based reference signals. In case the transmitted signal is derived from a space-based stable oscillator the measurement is said to be "one way"; while if the signal is transmitted from the ground and then transponded back by the spacecraft, the measurement is said to be "two way". The observed frequency shift (Doppler), as a function of time, indicates the relative motion between the spacecraft and the ground station ([20]).

3.1.1 Physical Model

According to the Doppler principle, if a frequency source moves respect to an observer, the frequency of the signal as received by the observer will be different from the frequency transmitted by the source. The physical model describing the Doppler shift is obtained starting from the following general relation, adapted from [21] in the case of a one way link (space to ground or viceversa):

$$\frac{f_A}{f_B} = \frac{d\tau_B}{d\tau_A} = \frac{d\tau_B}{dt_B}\frac{dt_B}{dt_A}\frac{dt_A}{d\tau_A} \tag{3.1}$$

where f_A and f_B are the frequencies measured at the link ends, while t and τ represent the coordinate and proper times, as defined in section 2.1.

As seen in Equation 3.1, the ratio between the two measured frequencies (at the ground and in space) is defined both in terms of the different proper time rates at the two locations ($\frac{d\tau_B}{dt_B}$ and $\frac{dt_A}{d\tau_A}$) and in terms of the purely geometric term $\frac{dt_B}{dt_A}$. The general proper time rate equation comes from general relativity and can be expressed in its most general form, according to [22], as:

$$\frac{d\tau}{dt} = \sqrt{-g_{\mu\nu}\frac{\dot{x}^\mu \dot{x}^\nu}{c^2}} \tag{3.2}$$

where $g_{\mu\nu}$ denotes Einstein's general relativity metric and $\dot{x}$ is the four velocity vector defined in the relativistic mechanics.

The coordinate time transfer ratio $\frac{dt_B}{dt_A}$ can be, instead, obtained by differentiating the quantity $t_B - t_A$ with respect to t_A. The general formulation of $t_B - t_A$, known as the light time equation, is adapted from [23]:

$$T_{AB} = t_B - t_A = \frac{|\boldsymbol{r}_B(t_B) - \boldsymbol{r}_A(t_A)|}{c} + \frac{\Delta_r}{c} \tag{3.3}$$

where $\boldsymbol{r}_B(t_B)$ and $\boldsymbol{r}_A(t_A)$ are the vector positions of A (transmitter) and B (receiver) in an Earth centered inertial frame, and the term $\frac{\Delta_r}{c}$ represents the light time correction which is actually a delay due to relativistic

effects.

In order to apply Equation 3.2 and Equation 3.3 to the specific project study of the RadioAstron Gravitational Redshift experiment, the components of both the metric tensor and the coordinate time transfer have to be written out according to the required level of accuracy. Since the gravitational redshift, as given by Equation 1.1, is in $\frac{1}{c^2}$, higher order terms can be neglected when developing $\frac{f_A}{f_B}$. In particular, Equation 3.2 becomes, after a Post Newtonian expansion of $g_{\mu\nu}$, according to Eq 3 from [21]:

$$\frac{d\tau}{dt} \approx \sqrt{1 - \frac{1}{c^2}(v^2 + 2U)} \approx 1 - \frac{1}{c^2}\left(\frac{v^2}{2} + U\right) \tag{3.4}$$

where v is the velocity module and U is the Newtonian potential with the convention $U > 0$.

Regarding the coordinate time transfer, its $\frac{1}{c^2}$ expansion is provided in [21] eq. 6:

$$T_{AB} \approx \frac{D_{AB}}{c} + \frac{\boldsymbol{D}_{AB} \cdot \boldsymbol{v}_B}{c^2} \tag{3.5}$$

where D_{AB} and $\boldsymbol{v}_B$ are respectively the distance between the link ends and the velocity of B, both computed at t_A.

Therefore $\frac{dt_B}{dt_A}$ follows by differentiating Equation 3.5:

$$\frac{dT_{AB}}{dt_A} = \frac{d(t_B - t_A)}{dt_A} = \frac{dt_B}{dt_A} - 1 = \frac{1}{c}\frac{dD_{AB}}{dt_A} + \frac{1}{c^2}\left(\frac{d\boldsymbol{D}_{AB}}{dt_A} \cdot \boldsymbol{v}_B + \boldsymbol{D}_{AB} \cdot \frac{d\boldsymbol{v}_B}{dt_A}\right) \tag{3.6}$$

Neglecting the acceleration term $\frac{d\boldsymbol{v}_B}{dt_A}$ and given:

$$D_{AB} = |\boldsymbol{r}_B(t_A) - \boldsymbol{r}_A(t_A)| = \sqrt{(x_B - x_A)^2 + (y_B - y_A)^2 + (z_B - z_A)^2} \tag{3.7}$$

$$\boldsymbol{D}_{AB} = D_{AB}\boldsymbol{n}_{AB} \tag{3.8}$$

$$\frac{dD_{AB}}{dt_A} = \frac{2\boldsymbol{D}_{AB} \cdot (\boldsymbol{v}_B - \boldsymbol{v}_A)}{2D_{AB}} = \boldsymbol{n}_{AB} \cdot (\boldsymbol{v}_B - \boldsymbol{v}_A) \tag{3.9}$$

$$\frac{d\boldsymbol{D}_{AB}}{dt_A} = \frac{d(D_{AB}\boldsymbol{n}_{AB})}{dt_A} = \frac{dD_{AB}}{dt_A}\boldsymbol{n}_{AB} + D_{AB}\frac{d\boldsymbol{n}_{AB}}{dt_A} \tag{3.10}$$

where $\boldsymbol{n}_{AB}$ is the unit vector from A to B, Equation 3.6 becomes:

$$\frac{dt_B}{dt_A} = 1 + \frac{\boldsymbol{n}_{AB} \cdot (\boldsymbol{v}_B - \boldsymbol{v}_A)}{c} + \frac{(\boldsymbol{v}_B \cdot \boldsymbol{n}_{AB})^2 - (\boldsymbol{v}_A \cdot \boldsymbol{n}_{AB})(\boldsymbol{v}_B \cdot \boldsymbol{n}_{AB})}{c^2} \tag{3.11}$$

neglecting the term $\frac{d\boldsymbol{n}_{AB}}{dt_A}$ when using Equation 3.10.

The extensive formula describing $\frac{f_A}{f_B}$ is then obtained by substituting Equation 3.4 and Equation 3.11 in Equation 3.1 and neglecting higher order terms:

$$\frac{f_A}{f_B} = \frac{1 - \frac{1}{c^2}\left(\frac{v_B^2}{2} + U_B\right)}{1 - \frac{1}{c^2}\left(\frac{v_A^2}{2} + U_A\right)}\left(1 + \frac{\boldsymbol{n}_{AB} \cdot (\boldsymbol{v}_B - \boldsymbol{v}_A)}{c} + \frac{(\boldsymbol{v}_B \cdot \boldsymbol{n}_{AB})^2 - (\boldsymbol{v}_A \cdot \boldsymbol{n}_{AB})(\boldsymbol{v}_B \cdot \boldsymbol{n}_{AB})}{c^2}\right) \approx$$

$$\approx \left[1 - \frac{1}{c^2}\left(\frac{v_B^2}{2} + U_B\right)\right]\left[1 + \frac{1}{c^2}\left(\frac{v_A^2}{2} + U_A\right)\right]\left(1 + \frac{\boldsymbol{n}_{AB} \cdot (\boldsymbol{v}_B - \boldsymbol{v}_A)}{c} + \frac{(\boldsymbol{v}_B \cdot \boldsymbol{n}_{AB})^2 - (\boldsymbol{v}_A \cdot \boldsymbol{n}_{AB})(\boldsymbol{v}_B \cdot \boldsymbol{n}_{AB})}{c^2}\right) =$$

$$= \left(1 + \frac{v_A^2 - v_B^2}{2c^2} + \frac{U_A - U_B}{c^2}\right)\left(1 + \frac{\boldsymbol{n}_{AB} \cdot (\boldsymbol{v}_B - \boldsymbol{v}_A)}{c} + \frac{(\boldsymbol{v}_B \cdot \boldsymbol{n}_{AB})^2 - (\boldsymbol{v}_A \cdot \boldsymbol{n}_{AB})(\boldsymbol{v}_B \cdot \boldsymbol{n}_{AB})}{c^2}\right) \approx$$

$$\approx 1 + \frac{\boldsymbol{n}_{AB} \cdot (\boldsymbol{v}_B - \boldsymbol{v}_A)}{c} + \frac{v_A^2 - v_B^2}{2c^2} + \frac{(\boldsymbol{v}_B \cdot \boldsymbol{n}_{AB})^2 - (\boldsymbol{v}_A \cdot \boldsymbol{n}_{AB})(\boldsymbol{v}_B \cdot \boldsymbol{n}_{AB})}{c^2} + \frac{U_A - U_B}{c^2} \tag{3.12}$$

therefore:

$$\frac{f_A}{f_B} = 1 + \frac{\boldsymbol{n}_{AB} \cdot (\boldsymbol{v}_B - \boldsymbol{v}_A)}{c} + \frac{v_A^2 - v_B^2}{2c^2} + \frac{(\boldsymbol{v}_B \cdot \boldsymbol{n}_{AB})^2 - (\boldsymbol{v}_A \cdot \boldsymbol{n}_{AB})(\boldsymbol{v}_B \cdot \boldsymbol{n}_{AB})}{c^2} + \frac{U_A - U_B}{c^2} \tag{3.13}$$

Given Equation 3.13, it is finally possible to compute the fractional frequency variation ($\Delta f/f$) in the case of a space to ground link as:

$$\frac{\Delta f}{f} = \frac{f_A - f_B}{f_B} = \frac{f_A}{f_B} - 1 = \frac{\boldsymbol{n}_{AB} \cdot (\boldsymbol{v}_B - \boldsymbol{v}_A)}{c} + \frac{v_A^2 - v_B^2}{2c^2} + \frac{(\boldsymbol{v}_B \cdot \boldsymbol{n}_{AB})^2 - (\boldsymbol{v}_A \cdot \boldsymbol{n}_{AB})(\boldsymbol{v}_B \cdot \boldsymbol{n}_{AB})}{c^2} + \frac{U_A - U_B}{c^2}$$
(3.14)

If the subscripts A and B are replaced respectively by e (Earth ground station) and s (satellite), the radial velocity of the spacecraft with respect to the ground station is defined as $\dot{D} = -\boldsymbol{n}_{AB} \cdot (\boldsymbol{v}_B - \boldsymbol{v}_A)$, $\boldsymbol{n}_{AB} = \boldsymbol{n}$ and $\frac{U_A - U_B}{c^2} = \frac{\Delta U}{c^2} = \frac{\Delta f_{grav}}{f}$, then Equation 3.14 agrees (omitting the ionospheric and tropospheric contributions but considering the clock offset) with eq.3 reported in [4]:

$$\frac{\Delta f_{1w}}{f} = -\frac{\dot{D}}{c} - \frac{v_s^2 - v_e^2}{c^2} + \frac{(\boldsymbol{v_s} \cdot \boldsymbol{n}) - (\boldsymbol{v_e} \cdot \boldsymbol{n})(\boldsymbol{v_s} \cdot \boldsymbol{n})}{c^2} + \frac{\Delta f_{grav}}{f} + \frac{\Delta f_0}{f} + O\left(\frac{v}{c}\right)^3$$
(3.15)

Regarding the two way Doppler measurements, the Doppler frequency shift can be easily derived starting from the one way formula. It is important to observe that, in this case, the gravitational effect on the frequency change is averaged out since the signal comes back to the original starting point where the gravitational potential is the same. The formula for the two way link is given here, according to [14]:

$$\frac{\Delta f_{2w}}{f} = -2\frac{\dot{D}}{c} - 2\frac{v_s^2 - v_e^2}{c^2} + \frac{|v_s^2 - v_e^2|}{c^2} - \frac{\boldsymbol{a_e} \cdot \boldsymbol{n}}{c}\Delta t + 2\frac{(\boldsymbol{v_s} \cdot \boldsymbol{n}) - (\boldsymbol{v_e} \cdot \boldsymbol{n})(\boldsymbol{v_s} \cdot \boldsymbol{n})}{c^2} + O\left(\frac{v}{c}\right)^3$$
(3.16)

where the acceleration term in this case is not neglected, being the light time Δt double respect to the one way measurement.

As introduced in section 1.3, the RadioAstron Gravitational Redshift experiment presents several challenges. First of all, the uncertainty in the spacecraft radial velocity is such that the corresponding Doppler shift error $\delta\dot{D}/c \sim 10^{-11}$ and this is considered worrying ([14]). Therefore, following the example of Gravity Probe A, one and two way data need to be combined in order to cancel the first order Doppler contribution ($1/c$). The compensation scheme results in:

$$\Delta f_{1w} - \frac{\Delta f_{2w}}{2} = \Delta f_{grav} + f(-\frac{|\boldsymbol{v_e^2} - \boldsymbol{v_s^2}|}{2c^2} + \frac{\boldsymbol{a_e} \cdot \boldsymbol{n}}{c}\Delta t) + \Delta f_0 + O\left(\frac{v}{c}\right)^3$$
(3.17)

where only the second order terms appear, together with the gravitational redshift which is not cancelled out.

There is however an additional technical challenge in the case of RadioAstron because the HDRRC complex is not able to operate in one and two way modes simultaneously. The three available synchronization modes are described in the following figure:
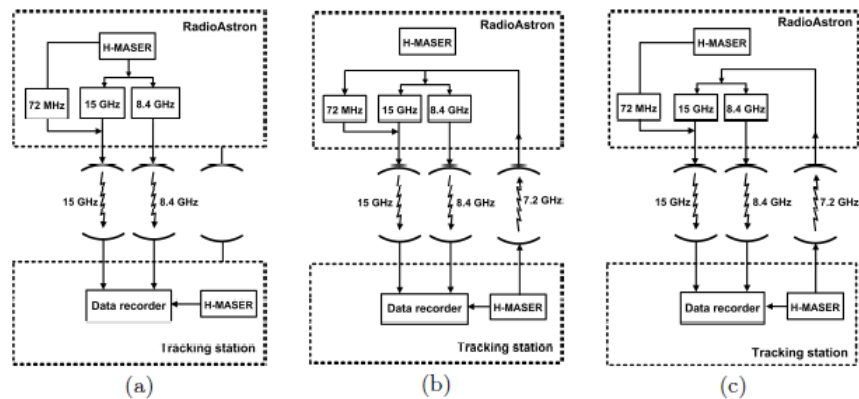
Figure 3.1: *Illustration of the RadioAstron onboard hardware synchroization schemes. (a) H-maser mode; (b) Coherent mode; (c) Semi-coherent mode. Scheme reported in [4].*

As seen from Figure 3.1, the H-maser and Coherent modes represent respectively the one and two way radio links. In the first one the signal sent from the spacecraft is locked to the SHM (Space H-maser) while in the second the signal from the tracking station is locked to the GHM (Ground H-maser). Finally the Semi-coherent mode is a hybrid between the H-maser and Coherent ones. In this operation scheme the uplink is phase locked

to the GHM as well as the 8.4 GHz and 15 GHz downlink carrier frequencies; however the modulation of the 15 GHz downlink carrier signal is phase locked to the SHM. Due to technical reasons the Semi-coherent mode has not been adopted for the experiment and the other two radio communication links are not able to work simultaneously. This technical problem is overcome with the "interleaving approach" which consists in combining one and two way frequency data by switching the operation mode every 4 minutes approximately ([4]). This enables to interpolate into the gaps with an acceptable error and use Equation 3.17.

The theory given so far in this section does not take into account a number of perturbing factors influencing the frequency measurements. When the signals encounter the atmosphere there are for instance several non negligible effects acting along their paths. Moreover, the radio equipment of both the spacecraft and the ground station has also an influence on the measurement accuracy. These factors determine noise, which is discussed in section 3.1.2.

3.1.2   Noise sources

The noise affecting the frequency measurements has both instrumental and natural causes, as introduced in section 1.3 with the terms Δf_{instr} and Δf_{media}. The former are characterized by ([24], [20]):

- Antenna mechanical noise (both transmitting and receiving)
- Radio-signal formation chain (amplifiers, frequency converters and so on)
- Phase modulation due to the transmitting antenna and spacecraft attitude and control noise
- On-board frequency oscillator
- Digital noise (rounding and so on) of the data handling/processing system

while the latter, instead, come from:

- Ionosphere
- Troposphere
- Interplanetary plasma

The aforementioned sources determine in principle both systematic and random errors. However, regarding the present project study, the dominating noise is represented by the onboard oscillator, considered to be the main responsible of the bias in the frequency observations, as stated with Equation 1.4. The problem is that the clock offset cannot be determined accurately enough because it would require knowledge of ε. The other items are assumed to be either negligible or "under control", meaning that their contributions are known. For instance the interplanetary plasma, given RadioAstron's orbit, does not represent any harm ([20], [24]) and can be completely excluded, as well as the digital noise is something that is absolutely under control if the processing algorithms are well thought. Moreover, the radio-signal formation chain, the phase modulation and the antenna mechanical noise can be assumed to bring random noise with zero mean and to be negligible respect to the ultra stable oscillator noise ([20]). According to [20] the mentioned sources of noise are below 10^{-15} (fractional frequency).

The ionospheric and tropospheric perturbations, on the other hand, have to be computed and taken into account when processing the frequency measurements because of the signal propagation through the Earth's atmosphere. The resulting uncancelled ionospheric and tropospheric noise, according to [4], has an order of magnitude of $1 - 2 \times 10^{-15}$ in terms of fractional frequency.

To sum up, the most relevant components of Δf_{instr} and Δf_{media} for the RadioAstron gravitational redshift experiment are the onboard frequency offset, the ionospheric and tropospheric noises. Since the biggest source of error is represented by the uncertainty of the H-maser offset between the ground stations and the spacecraft, an estimate of this is provided by the Allan deviation of the H-maser. This measure of frequency stability will be used as a reference to define the a priori statistical properties of the bias in one way frequency observations for the simulations study. Its definition is provided in section **??**.

3.1.3   Allan deviation

The Allan deviation mentioned in section 3.1.2, is the measure of frequency stability adopted to describe oscillators. ([25].

Given, from [25], the definitions of fractional frequency fluctuation $y(t)$ and fractional frequency average $\overline{y}_k$:

$$y(t) = \frac{\Delta f}{f} = \frac{\nu(t) - \nu_0}{\nu_0} = \frac{1}{2\pi\nu_0}\frac{d\phi}{dt} = \frac{dx}{dt} \tag{3.18}$$

$$\overline{y}_k = \frac{1}{\tau}\int_{t_k}^{t_{k+1}} y(t)dt = \frac{\phi(t_k + \tau) - \phi(t_k)}{2\pi\nu_0\tau} \tag{3.19}$$

where ν_0 is the nominal frequency, ϕ is the phase, $x = \frac{\phi(t)}{2\pi\nu_0}$, τ is the duration of the measurements, T is the time interval between the measurements and $t_{k+1} = t_k + T$; the Allan variance is defined as ([25]):

$$\sigma_y{}^2(\tau) = \langle \frac{(\overline{y}_{k+1} - \overline{y}_k)^2}{2} \rangle \tag{3.20}$$

with $T = \tau$. The angle brackets indicate the expected value operator.

The Allan deviation is simply the square root of $\sigma_y{}^2(\tau)$. This quantity is expressed in time domain, being a function of the averaging time τ. Based on the duration of the frequency observations, Equation 3.20 can then provide a good estimate of the uncertainty due to the adopted ultra stable oscillator.

3.2   Orbit Modeling

The equation of motion of a spacecraft orbiting the Earth is mainly described by the gravitational interactions between the spacecraft and the several celestial bodies influencing the motion of the satellite. In theory, as explained in the fundamental physics chapter, the correct way of studying the motion of a body consists of using the general form of the equation of motion in the curved spacetime defined by Einstein, which is Equation 2.13. However, for most applications of the Earth orbiting satellites, the relativistic effects on the orbital dynamics can be neglected (the speed of the spacecraft is much lower than the speed of light) and Newton's classical laws can be applied. Alongside with the gravitational phenomenon, there are in general also other effects to be considered, such as the atmospheric drag and the solar radiation pressure. In the following part of the section the reference formulas describing the spacecraft trajectory are given.

Since the Earth gravitational field has the biggest influence on RadioAstron, the motion of the satellite is expressed with respect to a non-rotating reference frame fixed to the centre of our planet (J2000 is the one adopted in the simulation software). This frame can be considered inertial when dealing with the short time intervals of the orbit determination process. The spacecraft motion with respect to the Earth is however perturbed by other bodies and therefore its acceleration can be expressed, making the simple preliminary assumption of point mass bodies, by:

$$\frac{d^2\boldsymbol{r}_s}{dt^2} = -G\frac{m_s + m_E}{r_s{}^3}\boldsymbol{r}_s + G\sum_{j\neq s,E} m_j \left(\frac{\boldsymbol{r}_j - \boldsymbol{r}_s}{r_{sE}{}^3} - \frac{\boldsymbol{r}_j}{r_s{}^3} \right) \tag{3.21}$$

where E denotes the Earth, s the satellite and j the other bodies. Equation 3.21 represents a very simplified case. In reality the perturbations due to the shape of the planet and its internal mass density distribution are not negligible and need to be taken into account. Therefore, the gravitational potential of the Earth may be expressed, in a body-fixed reference frame, as:

$$U = -\frac{\mu}{r} \left[1 - \sum_{n=2}^{\infty} J_n \left(\frac{R}{r} \right)^n P_n(\sin\phi) + \sum_{n=2}^{\infty} \sum_{m=1}^{n} J_{n,m} \left(\frac{R}{r} \right)^n P_{n,m}(\sin\phi)\cos m(\Lambda - \Lambda_{n,m}) \right] \tag{3.22}$$

where R is the Earth's mean equatorial radius, r the distance from the Earth's center of mass, ϕ is the geocentric latitude, Λ the longitude. $P_n(\sin\phi)$ are the so called Legendre Polynomials of degree n, $J_{n,m}$ and $\Lambda_{n,m}$ represent coefficients.

Equation 3.22 enables to describe the Earth's gravitational potential up to the desired level of accuracy, according to the application. Therefore, the first term on the right hand side of Equation 3.21 may be replaced by $-\boldsymbol{\nabla}U$. However, Equation 3.21 is defined in a non rotating frame so the spherical harmonics acceleration has to be expressed in accordance to the other terms of the equation. Moreover the gradient of U provides the acceleration in spherical coordinates so a coordinate transformation is also needed. These two steps are achieved by the transformation matrices $T_{r\phi\Lambda}^{xyz}$ and T_{xyz}^{XYZ}, so that:

$$\ddot{\boldsymbol{r}} = -T_{xyz}^{XYZ}T_{r\phi\Lambda}^{xyz}\boldsymbol{\nabla}U \tag{3.23}$$

where XYZ and xyz are respectively the inertial and body fixed frames (with rectangular coordinates), $\ddot{\boldsymbol{r}}$ is the complete acceleration exerted from the Earth.

The acceleration due to the solar radiation pressure force is generally described with this general expression:

$$\boldsymbol{f}_R = -C_R\frac{W_S A}{Mc}\boldsymbol{e}_S \tag{3.24}$$

where M is the satellite mass, A is the cross sectional area, C_R is the satellite reflectivity, W_S is the solar energy flux, $\boldsymbol{e}_S$ is the unit vector pointing to the Sun from the satellite and c the speed of light.

Concerning the perturbations due to the atmospheric drag, the acceleration is given by:

$$\boldsymbol{f}_D = -C_D\frac{1}{2}\rho\frac{A}{M}|\boldsymbol{\nu}|\boldsymbol{\nu} \tag{3.25}$$

where ρ is the atmospheric density, C_D is the drag coefficient, A is the reference area, M the mass of the satellite and $\boldsymbol{\nu}$ is the spacecraft velocity relative to the atmosphere.

To sum up, the equation of motion of the satellite can be expressed in its complete form as:

$$\frac{d^2\boldsymbol{r}_s}{dt^2} = \ddot{\boldsymbol{r}} + G\sum_{j\neq s,E} m_j \left(\frac{\boldsymbol{r}_j - \boldsymbol{r}_s}{r_{sE}{}^3} - \frac{\boldsymbol{r}_j}{r_s{}^3}\right) + \boldsymbol{f}_R + \boldsymbol{f}_D \tag{3.26}$$

The above mentioned equations are implemented in the Tudat software which enables to define both the environment (bodies involved), the level of detail regarding the accelerations due to each body and the reference frame in which the orbit is to be propagated. The integration of the equation of motion is carried out by means of a Runge Kutta Fehlberg method (RKF). This is a variable step size integrator that works by comparing two different RK approximations and choosing at each step the optimal step size according to a specified tolerance: if the two solutions do not agree within the specified level the step size is reduced, otherwise the approximation is accepted. If they agree up to a higher accuracy than specified, then the step size is increased.

An RK integrator is an integration method that consists of evaluating the derivative function at different points and times within the integration step, producing several approximations of the next function evaluation which are then averaged with certain weights. Using the notation adopted in chapter 4 of [5], given a differential equation of type $\dot{\boldsymbol{y}} = \boldsymbol{f}(t,\boldsymbol{y})$ with initial condition $\boldsymbol{y}(t_0) = \boldsymbol{y}_0$, its approximation at $t_0 + h$ may be expressed as:

$$\boldsymbol{y}(t_0 + h) \approx \boldsymbol{y}_0 + h\boldsymbol{\Phi} = \boldsymbol{\eta}(t_0 + h) \tag{3.27}$$

where h is the step size, $\boldsymbol{\Phi}$ is the increment function and $\boldsymbol{\eta}$ represents the approximation function.
Given Equation 3.27, it is possible to define the local truncation error:

$$e_{RK} = |\boldsymbol{y}(t_0 + h) - \boldsymbol{\eta}(t_0 + h)| \leqslant const \cdot h^p \tag{3.28}$$

with p being the order of the truncation error (h is assumed to be a very small quantity).

The general s-order Runge Kutta formula implies s function evaluations which define the increment function. Several coefficients (c, a, b) are involved in the process:

$$\boldsymbol{k}_1 = \boldsymbol{f}(t_0 + c_1 h, \boldsymbol{y}_0) \tag{3.29}$$

$$\boldsymbol{k}_i = \boldsymbol{f}(t_0 + c_i h, \boldsymbol{y}_0 + h\sum_{j=1}^{i-1} a_{ij}\boldsymbol{k}_j) \qquad (i = 2...s) \tag{3.30}$$

$$\boldsymbol{\Phi} = \sum_{i=1}^{s} b_i \boldsymbol{k}_i \tag{3.31}$$

The coefficients are chosen in order to maximize the order of the local truncation error defined in Equation 3.28.

The order of the RK integrator (and thus the number of coefficients), are chosen according to the required accuracy of the application. This integration method is available in the Tudat software. The dynamical model chosen for RadioAstron OD simulations and the settings adopted for the numerical integration of the equation of motion are given in chapter 4.

According to the theory of the least squares estimation algorithm, explained in section 3.3 when dealing with the orbit determination process, the dynamical model is absolutely perfect and represents reality without any error. However, in practice, this is never true since the several perturbations acting on the satellites cannot be perfectly modelled. In the case of RadioAstron OD simulations this aspect is discussed in section 4.1 where the simulation concept is described.

3.3 Orbit Determination

The orbit determination aspect plays a fundamental role in the RadioAstron Gravitational Redshift Experiment: the state vector parameters of the satellite (especially the velocity components) affect the Doppler equations in a significant way, as seen in section 3.1. As stated in the introduction, the orbit of RadioAstron is not easy to determine due to the several perturbation sources. Not only is the satellite orbit highly perturbed by the Moon and by the solar radiation pressure, but also by the unloadings of the reaction wheels performed several times a day (as reported in [11]). The process described in this chapter is the least squares algorithm which is going to be used in the software for the orbit determination simulations.

Given a set of measurements and a reference trajectory, the algorithm provides a solution which best fits the observations by minimizing the square of the residuals between the computed trajectory and the measurements. The initial set of parameters is then updated according to the solution provided by the algorithm. The two

analytical models that are involved in this process are the dynamical and the observation model. Therefore assumptions about the dynamics of the satellite are very important, as well as assumptions on the noise profile affecting the observations.

3.3.1 Linearization of the estimation problem

From now on, the vector of estimated parameters will be indicated with $\boldsymbol{X}$ and the vector of observations with $\boldsymbol{Y}$. In orbit determination problems $\boldsymbol{X}$ is usually characterized by at least 6 variables representing the satellite state vector (position and velocity in an Earth centered inertial reference frame); while the observation vector generally comprises all the kinds of measurements that are computed during the time interval of the estimation. In the specific case of the RadioAstron Gravitational Redshift experiment, the observations consist of Doppler measurements, as described in section 3.1. During the following theory explanation, both $\boldsymbol{X}$ and $\boldsymbol{Y}$ will be treated in a general way, without specifying their exact number of components and which parameters are estimated together with the satellite state vector (position and velocity).

The time evolution of the vector of estimated parameters, according to [5], can be described as an ordinary differential equation:

$$\dot{\boldsymbol{X}} = F(\boldsymbol{X}, t) \tag{3.32}$$

with $\boldsymbol{X}$ made of n variables; and the observations can be expressed through an analytical model G plus an uncertainty ϵ:

$$\boldsymbol{Y}_i = G(\boldsymbol{X}_i, t_i) + \boldsymbol{\epsilon}_i \tag{3.33}$$

for $l = 1, ... l$ and with $\boldsymbol{Y}_i$ being a vector of p components (measurements) referred to t_i, and $\boldsymbol{\epsilon}_i$ representing the vector of the observation errors at $t = t_i$.

Assuming $\boldsymbol{X}^*(t)$ to be a reference solution (based on a priori information) and $\boldsymbol{X}(t)$ the true one, a linearization process can be implemented:

$$\dot{\boldsymbol{X}}(t) \approx F(\boldsymbol{X}^*, t) + \left[\frac{\partial F(t)}{\partial \boldsymbol{X}(t)}\right]^* [\boldsymbol{X}(t) - \boldsymbol{X}^*(t)] \tag{3.34}$$

$$\boldsymbol{Y}_i = G(\boldsymbol{X}_i, t_i) + \boldsymbol{\epsilon} \approx G(\boldsymbol{X}_i^*, t_i) + \left[\frac{\partial G(t)}{\partial \boldsymbol{X}}\right]_i^* [\boldsymbol{X}(t_i) - \boldsymbol{X}^*(t_i)] + \boldsymbol{\epsilon}_i \tag{3.35}$$

where $\left[\frac{\partial F(t)}{\partial \boldsymbol{X}(t)}\right]^*$ and $\left[\frac{\partial G(t)}{\partial \boldsymbol{X}(t_i)}\right]^*$ are respectively an $n \times n$ and $p \times n$ matrices characterized by the derivatives of the dynamical and measurement models with respect to the state vector, computed at $\boldsymbol{X}(t) = \boldsymbol{X}^*(t)$.

If, according to [26], the variables $\boldsymbol{x}$ and $\boldsymbol{y}$ are defined as follows:

$$\boldsymbol{x}(t) = \boldsymbol{X}(t) - \boldsymbol{X}^*(t) \tag{3.36}$$

$$\boldsymbol{y}_i = \boldsymbol{Y}(t_i) - \boldsymbol{Y}^*(t_i) = \boldsymbol{Y}(t_i) - G(\boldsymbol{X}_i^*, t_i) \tag{3.37}$$

then Equation 3.34 and Equation 3.35 can be written in a more simple and concise way:

$$\dot{\boldsymbol{x}}(t) = A(t)\boldsymbol{x}(t) \tag{3.38}$$

$$\boldsymbol{y}_i = \tilde{H}_i \boldsymbol{x}_i + \boldsymbol{\epsilon}_i \tag{3.39}$$

with:

$$A(t) = \left[\frac{\partial F(t)}{\partial \boldsymbol{X}(t)}\right]^* \tag{3.40}$$

and:

$$\tilde{H}_i = \left[\frac{\partial G(t)}{\partial \boldsymbol{X}}\right]_i^* \tag{3.41}$$

The next step is now to relate the observations to a particular epoch state. To do so, the concept of state transition matrix is first explained in subsection 3.3.2. Be aware that the term "state" is adopted in this mathematical treatment to identify the general vector of estimated parameters $\boldsymbol{X}$ and is not necessarily referred only to the position and velocity of the spacecraft.

3.3.2 State transition matrix

The state transition matrix is a matrix that relates the states of two different epochs. It is defined by the following relation ([26]):

$$\boldsymbol{x}(t) = \Phi(t, t_k)\boldsymbol{x}_k \tag{3.42}$$

where $\boldsymbol{x}_k = \boldsymbol{x}(t = t_k)$.

The matrix $\Phi(t_i, t_k)$ is called the state transition matrix and connects the state at $t = t_k$ with the state at $t = t_i$. The main properties of this matrix are:

- $\Phi(t_k, t_k) = I$
- $\Phi(t_i, t_k) = \Phi(t_i, t_j)\Phi(t_j, t_k)$
- $\Phi(t_i, t_k) = \Phi^{-1}(t_k, t_i)$

where I is the identity matrix.

Given the definition of Φ, it follows that:

$$\dot{\boldsymbol{x}}(t_i) = \dot{\Phi}(t_i, t_k)\boldsymbol{x}_k \tag{3.43}$$

therefore, using Equation 3.38, it follows:

$$\dot{\Phi}(t, t_k)\boldsymbol{x}_k = A(t)\Phi(t, t_k)\boldsymbol{x}_k \tag{3.44}$$

with:

$$\dot{\Phi}(t, t_k) = A(t)\Phi(t, t_k) \tag{3.45}$$

and the initial condition is given by the first property of the state transition matrix $\Phi(t_k, t_k) = I$.

The procedure to compute the inverse of the state transition matrix is explained in detail in [26] but will not be treated here extensively.

From [5], another equivalent and more direct way of defining the state transition matrix can be found:

$$\Phi(t, t_0) = \frac{\partial \boldsymbol{x}(t)}{\partial \boldsymbol{x}(t_0)} \tag{3.46}$$

The state transition matrix is an important tool that enables to connect the observations of one epoch to the initial state. This is explained in subsection 3.3.3.

3.3.3 Relation between observations and epoch state

After defining the state transition matrix, Equation 3.39 can be written in the more complete form, as a function of the state at $t = t_0$ which is the initial epoch:

$$\boldsymbol{y}_i = \tilde{H}_i \Phi(t_i, t_0)\boldsymbol{x}_0 + \boldsymbol{\epsilon}_i \tag{3.47}$$

In this way everything is reconducted to the initial state and the number of unknowns in the system is significantly reduced.

More simply, the whole system of equations can be expressed in a more compact way as follows:

$$\boldsymbol{y} = H\boldsymbol{x}_0 + \boldsymbol{\epsilon} \tag{3.48}$$

where the observation vectors of all the epochs are concatenated into $\boldsymbol{y}$ and $H = \tilde{H}\Phi(t, t_0)$.

At this point the solution approach of the least squares method can be described. This is done in the next subsection.

3.3.4 Least Squares Solution

The least squares criterion consists of choosing the state estimate which minimizes the sum of the squares of the residuals with respect to the observations. Formally, it is the solution which minimizes the loss function J ([26]), reported here in its basic form (without weighting the observations):

$$J(\boldsymbol{x}_0) = \frac{1}{2}\boldsymbol{\epsilon}^T\boldsymbol{\epsilon} \tag{3.49}$$

with $\boldsymbol{x}_0$ being the initial state vector and $\boldsymbol{\epsilon}$ representing the difference between modelled and measured observations.

In other words it is the solution which "best fits" the observations, meaning that the square of the difference between the modeled observations and the actual measurements is as small as possible ([5]). To this extent, Figure 3.2 provides a clear illustration of the approach:
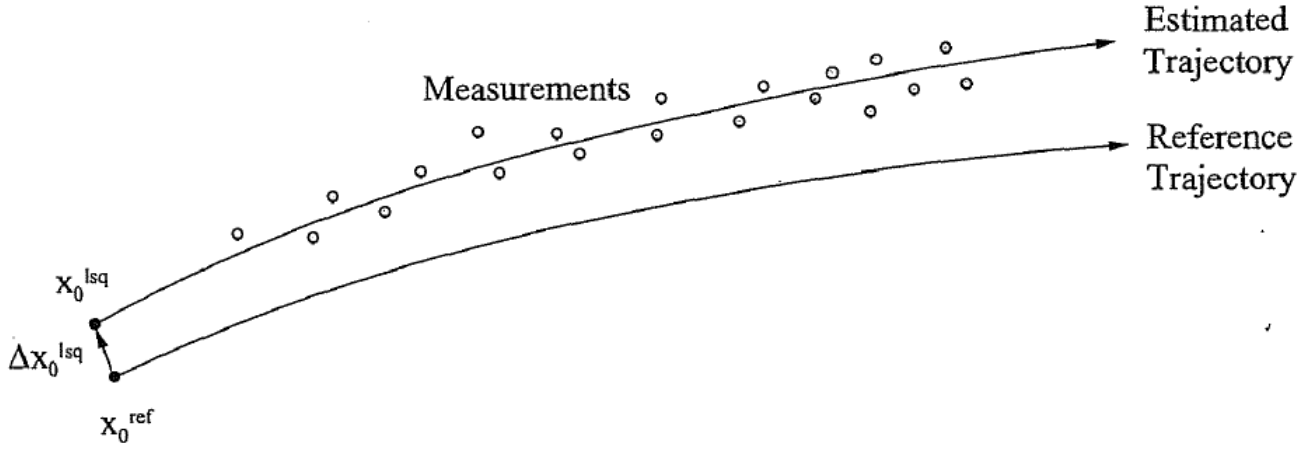
Figure 3.2: *Least squares orbit determination approach. Figure taken from [5]*

As seen in the illustrative scheme of Figure 3.2, starting from a reference trajectory, its parameters are corrected with the purpose of finding the best fit of the observations.

In order to minimize the loss function expressed by Equation 3.49, if the columns of H are linearly independent, then the minimum is uniquely identified by the condition:

$$\frac{\partial J(\boldsymbol{x}_0)}{\partial \boldsymbol{x}_0} = 0 \tag{3.50}$$

This condition implies, according to [5], that the general solution of the least squares problem is, if all observations have equal weight:

$$\hat{\boldsymbol{x}}_0 = (H^T H)^{-1}(H^T \boldsymbol{y}) \tag{3.51}$$

where the hat symbol indicates the least squares estimate. Therefore, the least squares solution is, according to the symbols adopted so far:

$$\hat{\boldsymbol{X}}_0 = \boldsymbol{X}_0^{ref} + \hat{\boldsymbol{x}}_0 \tag{3.52}$$

Since the solution provided by Equation 3.52 has been obtained by means of a linearization process, the described method needs to be iterated in order to improve the accuracy of the estimation:

$$\boldsymbol{X}_0^{j+1} = \boldsymbol{X}_0^{j} + \hat{\boldsymbol{x}}_0^{j} \tag{3.53}$$

The iterations can be stopped according to the accuracy level that one wants to achieve. A measure of the level of accuracy of the estimation is, for instance, the absolute difference between the solutions provided by two successive iterations.

3.3.5 Weighted Least Squares

In the standard least squares approach described so far, all the observations have the exact same weight and are treated in the same way. In the weighted least squares, instead, each observation is weighted according to its mean measurement error, indicated with σ_i (in principle this shall include both random and systematic errors). Therefore each residual $\boldsymbol{y}_i$ is normalized respect to σ_i:

$$\bar{\boldsymbol{y}}_i = \frac{\boldsymbol{y}_i}{\sigma_i} \tag{3.54}$$

The final solution of the weighted least squares becomes then, assuming that H is always full rank ([5]) and that the measurements are uncorrelated:

$$\hat{\boldsymbol{x}}_0 = (H^T W H)^{-1}(H^T W \boldsymbol{y}) \tag{3.55}$$

where $W = \text{diag}(\sigma_1^{-2}, ..., \sigma_n^{-2})$.

In case the measurements noise is white Gaussian (this will be actually the assumption made for the simulations study described in section 4), the terms characterizing the weighting matrix W will correspond to the measurements standard deviations. The σ values appearing in Equation 3.54 and in Equation 3.55 through W are therefore, conceptually speaking, different. In Equation 3.54 they are the theoretical measurement uncertainties while in the weighting matrix of Equation 3.55 they appear under certain assumptions.

3.4 Postfit uncertainty

Once the weighted least squares fit is obtained, the computed solution will still be affected by errors due to the uncertainty in the measurements. To express the least squares solution as a function of the measurements uncertainty vector $\boldsymbol{\epsilon}$ ([5]) the following relationship holds:

$$\hat{\boldsymbol{X}}_0 = \boldsymbol{X}_0^{ref} + (H^T W H)^{-1}(H^T W \boldsymbol{y}) = \boldsymbol{X}_0 + (H^T W H)^{-1}(H^T W \boldsymbol{\epsilon}) \qquad (3.56)$$

where it is clear that the solution provided by the least squares differs from the true one only because of $\boldsymbol{\epsilon}$.

In order to study the statistical properties of the solution in terms of its uncertainty, it is very useful to compute its expected value and covariance:

$$E(\hat{\boldsymbol{X}}_0) = \boldsymbol{X}_0 + (H^T W H)^{-1}(H^T W E(\boldsymbol{\epsilon})) \qquad (3.57)$$

$$Cov(\hat{\boldsymbol{X}}_0, \hat{\boldsymbol{X}}_0) = E((\hat{\boldsymbol{X}}_0 - E(\hat{\boldsymbol{X}}_0))(\hat{\boldsymbol{X}}_0 - E(\hat{\boldsymbol{X}}_0))) \qquad (3.58)$$

If the measurements errors are assumed to be only random (thus neglecting the systematic component), the expected value of the least squares estimate is exactly the true solution, according to Equation 3.57. In fact, in this case $E(\epsilon) = 0$. If this assumption is valid, then the covariance of the least squares solution can be written as ([5]):

$$Cov(\hat{\boldsymbol{X}}_0, \hat{\boldsymbol{X}}_0) = (H^T W H)^{-1}(H^T W)E(\boldsymbol{\epsilon}\boldsymbol{\epsilon}^T)(W H)(H^T W H)^{-1} \qquad (3.59)$$

Moreover, if the measurement errors are considered uncorrelated and the weighting matrix is defined as in subsection 3.3.5, it follows that $W^{-1} = E(\boldsymbol{\epsilon}\boldsymbol{\epsilon}^T)$ and thus Equation 3.59 can be simplified as:

$$Cov(\hat{\boldsymbol{X}}_0, \hat{\boldsymbol{X}}_0) = (H^T W H)^{-1} \qquad (3.60)$$

Once the covariance matrix is computed, the square root of the diagonal terms of the matrix will consist of the standard deviations of the components of $\hat{\boldsymbol{X}}_0$, while the other terms of the matrix (off-diagonal) are a measure of the correlation between the errors of the individual components.

Concerning the accuracy of the least squares solution, it is important to underline that both $\hat{\boldsymbol{X}}_0$ and $\boldsymbol{\epsilon}$ are treated as random variables and therefore the expected value and the covariance of $\hat{\boldsymbol{X}}_0$ define an interval in which the solution is most likely to be found. The following picture provides an illustration of this concept:
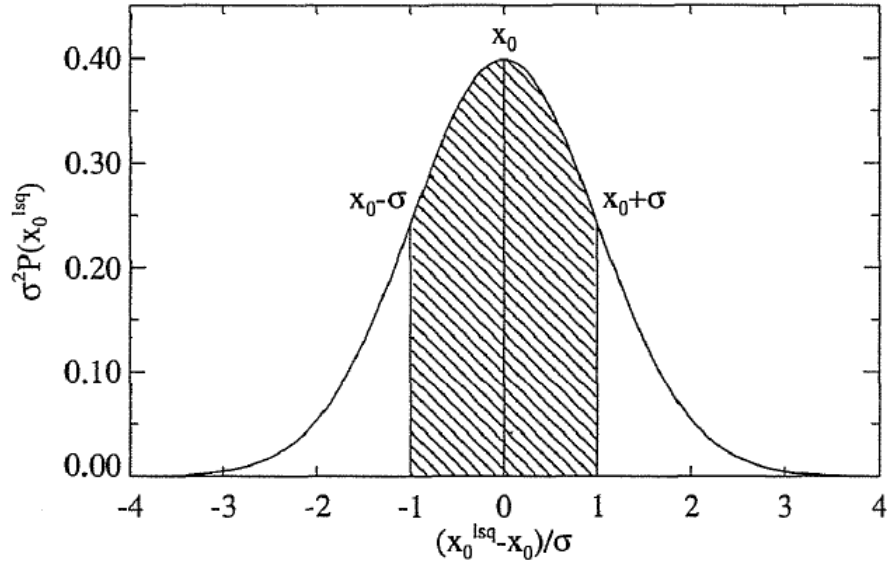
Figure 3.3: *Probability distribution of the least squares solution, assuming that the errors have a normal distribution. Figure from [5]*

In Figure 3.3, the marked area corresponds to a probability of 67%.

The assumption of uncorrelated white Gaussian noise, represented by Figure 3.3, is one of the main assumptions on which the simulations study described in section 4 is based. Although this is a very optimistic assumption (it represents an ideal situation), the contribution of systematic errors in the observations will not be neglected in the simulations study. It will be treated with a proper selection of the estimated parameters, as well as with the help of a consider covariance study. The mathematical theory of these topics is given in section 3.4.1.

3.4.1 Contribution of systematic errors and consider covariance

Systematic errors may come from uncertainties in the dynamical model, biases in observations, errors in the ground stations locations and so on. In order to deal with this issue one can choose, for instance, to extend the list of estimated parameters according to the specific needs. As an example, if observations are known to be biased and this contribution is expected to be relevant (as in the case of RadioAstron Gravitational Redshift experiment), the systematic error can be estimated as an additional parameter. The same can be said, for instance, with respect to the radiation pressure coefficient.

However, despite the choice of estimating additional parameters, the impact of unmodeled systematic errors on the covariance computation can be described through the consider covariance matrix. This mathematical approach is useful when studying the impact of uncertainties of non estimated parameters characterizing the measurement model. They are considered to be uncertain but their values are not updated at each iteration of the least squares algorithm.

Given the vector of consider parameters, represented as $\boldsymbol{C}$, Equation 3.33 can be rewritten as:

$$\boldsymbol{Y}_i = G(\boldsymbol{X}_i, \boldsymbol{C}, t_i) + \boldsymbol{\epsilon}_i \tag{3.61}$$

which is approximated by:

$$\boldsymbol{y}_i \approx H_{ix}\boldsymbol{x}_0 + H_{ic}\boldsymbol{c} + \boldsymbol{\epsilon}_i \tag{3.62}$$

where H_x and H_c denote the derivatives of the observation model with respect to the state vector $\boldsymbol{X}$ and the consider parameters vector $\boldsymbol{C}$. $\boldsymbol{Y}$ and $\boldsymbol{y}$ are always linked by the relation $\boldsymbol{y}_i = \boldsymbol{Y}_i - G(\boldsymbol{X}_i^*, t_i)$.

In this case the least squares solution may be written as ([5]):

$$\hat{\boldsymbol{X}}_0 = \boldsymbol{X}_0 + (H_x^T W H_x)^{-1} H_x^T W (H_c \boldsymbol{c} + \boldsymbol{\epsilon}) \tag{3.63}$$

If the consider parameters $\boldsymbol{c}$ are assumed to be random quantities with zero mean, the expected value of the least squares estimation will still be the true solution $\boldsymbol{X}_0$.

Regarding the covariance of the solution with the consider parameters, it is given by ([5]):

$$P^c = (P H_x^T W)(H_c C H_c + E(\boldsymbol{\epsilon}\boldsymbol{\epsilon}^T))(P H_x^T W)^T = P + (P H_x^T W)(H_c C H_c^T)(P H_x^T W)^T \tag{3.64}$$

where $P = (H_x^T W H_x)^{-1}$ and $W^{-1} = E(\boldsymbol{\epsilon}\boldsymbol{\epsilon}^T)$, and C is the covariance of the consider parameters, so $C = E(\boldsymbol{c}\boldsymbol{c}^T)$.

Even if both $\boldsymbol{\epsilon}$ and $\boldsymbol{c}$ are assumed to be random variables with zero mean, their impact on the solution is very different. Measurement errors affect the single orbit determination creating a certain noise which decreases as a function of the number of observations (assuming white Gaussian noise). On the other hand, the impact of consider parameters is constant and does not decrease with increasing data (see Equation 3.64).

When applying least squares methods, in order to speed up the convergence process and improve the estimation, it is very useful to use some a priori information about the covariance of $\boldsymbol{X}$. The estimation with a priori information will be discussed in the next subsection.

3.4.2 Estimation with a priori information

When some a priori information on the uncertainty of $\boldsymbol{X}$ is available, the estimation approach consists of using a modified loss function to minimize for the computation of the least squares solution. In particular, given $\boldsymbol{x}_0^{apr} = \boldsymbol{X}_0 - \boldsymbol{X}_0^{apr}$, the new loss function (assuming first the case with no weighting) will be ([5]):

$$J = (\boldsymbol{x}_0^{apr})^T \Lambda \boldsymbol{x}_0^{apr} + (\boldsymbol{y} - H\boldsymbol{x}_0)^T (\boldsymbol{y} - H\boldsymbol{x}_0) \tag{3.65}$$

where $\Lambda = {P_0^{apr}}^{-1}$.

The minimization of Equation 3.65, according to [5], brings:

$$\hat{\boldsymbol{x}}_0 = (\Lambda + H^T H)^{-1} (\Lambda \boldsymbol{x}_0^{apr} + H^T \boldsymbol{y}) \tag{3.66}$$

In the case of a weighted least squares, the solution instead becomes:

$$\hat{\boldsymbol{x}}_0 = (\Lambda + H^T W H)^{-1} (\Lambda \boldsymbol{x}_0^{apr} + H^T W \boldsymbol{y}) \tag{3.67}$$

where W is the weighting matrix.

In conclusion, the relation between the estimated covariance and the a priori covariance is given by ([5]):

$$P_0^{-1} = (P_0^{apr})^{-1} + (H^T W H) \tag{3.68}$$

This approach speeds up the estimation process and enables to improve the final estimation. The use of a priori information in the simulations study described in chapter 4 represents an extremely important tool. Both formal errors and correlations of the parameters involved in the present project study of RadioAstron Gravitational Redshift experiment are highly influenced by the a priori constraints given to certain variables, such as the biases in one way frequency observables. This topic is treated in detail in section 5.3.

Chapter 4

RA Doppler measurements and simulations of their statistics

This chapter describes the principles of the simulations study performed to support the gravitational redshift experiment with RadioAstron. In section 4.1 the simulation concept and the goals of the project study are explained, with references to the research questions of section 1.6. The assumptions under which the Doppler measurements are generated and the orbit determination is carried out are then discussed in section 4.2, followed by the adopted settings reported in section 4.3. Finally, section 4.5 is dedicated to the verification and validation of the implemented simulations.

4.1 Simulation concept and parameters choice

The simulations study aims to reproduce the estimation of the EEP violation parameter by means of an orbit determination process (including ε in the list of parameters) resembling the real experiments conditions. The goal is to perform a covariance analysis to study how the uncertainties of the several parameters involved in the RadioAstron gravitational redshift experiment impact the EEP violation parameter estimation. The orbit determination simulation process is carried out through a least squares algorithm implementation, based on the theory described in section 3.3. The most important output of the simulations study is represented by the ε formal error which enables to answer the main research question about the accuracy of the experiment.

Some parameters involved in Equation 3.17, as the spacecraft state vector and Δf_0, cannot be determined accurately enough without making use of Equation 1.1, which requires knowledge of ε. With respect to this issue, the concept of performing an orbit determination analysis including the EEP violation parameter provides useful statistical knowledge for a more precise description of the experiment error budget. More exactly, the correlations with ε can be computed, as well as the $\delta\varepsilon$ as a function of the parameters uncertainties and the observations noise.

The choice of the parameters to estimate in the simulations study is the first step towards the implementation of the least squares multi-arc orbit determination process. The main criterion driving this choice consists of selecting the most suitable parameters to resemble the realistic uncertainties faced in the experiment. At the same time, attention must be paid to the number of parameters itself: a very high number might bring numerical issues in the process of the covariance matrix computation, while a very small number leads to unrealistic simulation results.

Given the main research questions of section 1.6, the spacecraft state vector parameters and ε are obviously estimated for every experiment time interval. Position and velocity, in fact, contribute in big part to the terms of the compensation scheme adopted for the processing of frequency measurements (Equation 3.17) and describe the motion of the spacecraft.

Regarding the orbital dynamics of RadioAstron, however, as described in section 1.2, there are a number of relevant perturbing effects acting on the spacecraft, such as the gravitational perturbation of the Moon, the solar radiation pressure and the stabilization thrusters effect during the reaction wheels unloading. Although the ST firings occur several times a day and are an important short term perturbing effect of the satellite center of mass ([11]), during the gravitational redshift experiment sessions no unloadings were performed. Therefore they are not considered in the simulation of the RadioAstron dynamical model so no additional parameters related to the Δvs induced by the thrusters are needed. On the other hand, solar radiation pressure cannot be neglected as well as, indeed, the Moon. In [11] it is shown that, when performing RadioAstron's orbit reconstruction from observations, the type of SRP acceleration model adopted in the estimation has a strong impact on the quality of the measurements fit. The best accuracy is reached with an analytical model characterized by 3 different coefficients, while a model with only one coefficient produces the biggest error. This uncertainty needs

to be taken into account in the simulations of the gravitational redshift experiment. The only available model in Tudat is the cannonball, described by Equation 3.24, which is indeed not realistic. However, for a correct estimation of $\delta\varepsilon$ in the simulations it is important to resemble only the uncertainty of the adopted model. A preliminary study was then conducted to verify the goodness of the simulated spacecraft dynamical model by fitting real satellite estimated position data provided by the RA navigation support team, as described in section 4.5.1. The radiation pressure coefficients settings and statistical properties were chosen according to the verification outcome and are summarized in section 4.3. The option of estimating empirical accelerations has been investigated as well but has been rejected for the nominal simulations study. They would consist of 3 parameters for each time arc (given the experiments durations of roughly one hour and the spacecraft orbit, only the constant terms would be estimated) against 1 parameter only in the case of the radiation pressure coefficient. Moreover, comparisons between simulations run in both ways (once with radiation pressure coefficient and once with empirical accelerations) applying the same settings have brought the same results for ϵ.

Regarding the observation model parameters, the discussion related to the noise affecting the measurements, given in section 3.1.2, supported by the structure of Equation 3.17, strongly suggests to estimate a bias in one way frequency links. This bias is assumed to be equal to the clock (H-maser) offset between the ground and space based systems and thus it has an absolute nature (it is additive). In particular, since Δf_0 changes in time and there are several different stations involved in the experiments, it is assumed that for each arc and for each station there is a different bias. The number of biases is then a function of the number of ground stations and the number of different experiment time intervals. The uncertainty of the frequency offset is supposed to be a limiting factor for the experiment accuracy so the estimation of this parameter is extremely important.

An uncertainty in the geodetic position of the Pushchino station, the main RadioAstron operational ground-based station, has been suspected as a source of significant contribution in the overall noise budget of the experiment. Therefore the coordinates of the TS have been included in the list of parameters. This problem has also been investigated in a deeper way with the performance of a consider covariance analysis which is reported in section 5.2.

To sum up, the chosen set of parameters to estimate is summarized as follows:

- Initial state vector parameters for each arc
- Arc-wise radiation pressure coefficients (C_R)
- EEP violation parameter (always referred to as ε and estimated over the whole time span in which experiments are carried out, being it considered as an independent and unique fundamental physics parameter)
- Pushchino station coordinates (cartesian)
- Arc-wise biases in one way observations for each ground station

4.2 Assumptions

The main assumptions concerning the simulations structure are reported below:

- Each arc is statistically independent of the others. This means that the a priori covariance of the parameters at the beginning of each experiment time interval is not obtained by propagating the covariance computed at previous times but it is chosen independently. The selected a priori uncertainty values are the same at the beginning of every arc. A priori orbital data for the initial guess are taken from the RadioAstron reconstructed orbit files. This data is available from [12].
- All ground stations involved have no uncertainty in their position, except PU for which an a priori standard deviation of 10 meters per each coordinate is set. Since 10 meters is the accuracy that can be reached with a normal GPS device, this value was not increased.
- Two way observations are unbiased. Although this assumption is not completely true in reality, it is still representative of the real situation. The most relevant contribution to the bias in observations is the onboard H-maser offset which appears in the one way Doppler equation but not in the two way model (see Equation 3.15). Therefore, if other effects contributing to the bias are neglected, it is fine to assume that two way observations are unbiased.
- Bias in one way observations is an absolute bias and is different for every station and every time arc. The bias is assumed to be constant throughout one experiment duration (about one hour).
- Measurements are generated every second. One and two way Doppler observations are simulated at the same time. Regarding the time spacing of the observations, to speed up the process of the simulations, sometimes it was increased to 10 seconds making use of the property of Gaussian random variables according to which noise decreases following the curve $1/\sqrt{N}$ (with N being the number of measurements).
- Noise is assumed to be uncorrelated white Gaussian.
- The non-gravitational perturbations in the dynamics of RadioAstron are represented by the solar radiation pressure force (cannonball model), the coefficient of which is estimated arc-wise. The perturbations due to the unloadings of the reaction wheels are neglected.

The specific simulations settings are reported in section 4.3.

4.3 Simulation Settings

The RadioAstron simulated orbital motion is set up considering the gravitational influence of the Earth (spherical harmonic coefficients up to degree and order 8), the Sun, Moon, Mars and Jupiter. The acceleration exerted by the Sun consists of the radiation pressure component too. To model this influence the cannonball model, as given by Equation 3.24, is adopted with a cross sectional area of $100m^2$, a mass of $3600kg$ and a radiation pressure coefficient set to 1.45. The acceleration settings adopted to propagate the orbit of RadioAstron are summarized in Table 4.1 and the satellite parameters in Table 4.2.

Table 4.1: Acceleration settings

Body	Type of acceleration exerted from the body
Earth	Spherical Harmonics, degree and order 8
Sun	Central gravity and radiation pressure
Moon	Central gravity
Mars	Central gravity
Jupiter	Central gravity

Table 4.2: Satellite parameters

Satellite parameters	Value
Mass	3600 Kg
Cross sectional area	$100m^2$
C_R	1.45

The estimates of lunar and planetary orbits are provided in the Tudat software by DE421 Ephemeris. All data is expressed in the J2000 inertial reference frame, in which the spacecraft orbit is defined, and the adopted time standard in the software is Terrestrial Time (TT). The Cowell propagation method and a Runge Kutta with variable step size integrator type (RKF78) are applied for the numerical integration. The minimum and maximum time steps were fixed respectively to $0.0001s$ and $100s$, based on the knowledge that the spacecraft motion experiences rapid changes at perigee compared to its apogee passages.

For the simulations of one and two way Doppler measurements, the generated observable in the software is the fractional frequency fluctuation $\frac{\Delta f}{f}$ and the frequency ratio is expressed with terms up to the second order in $\frac{1}{c}$, according to the formulas described in section 3.1.1.

The time intervals (arcs) and the ground stations chosen for the simulation of the orbit determination process are the ones corresponding to the real experiment scenarios. The experiments selected for the simulations study, together with the starting time, stations and durations of the observations, are reported in Table 4.3. A set of 15 experiments was chosen, in order to find a compromise between a consistent number of observations and the required computational time to run the simulations and perform post processing analysis. The coordinates adopted for each station are reported in Table 4.5 and the full list of the real experiment sessions is provided in Table 4.4.

Table 4.3: *Experiments selected for the simulations study*

Experiment code	Start Time (UTC)	Stations	Duration (s)
raks13ab el053a	24/10/2015 14:00:00	Ef On Sv Wn Wz Zc	3600
raks13ac el053b	25/10/2015 14:00:00	Ef On Sv Wn Wz Zc	3600
raks13ad el053c	31/10/2015 22:00:00	Ef On Sv Wn Wz Zc	3600
raks13ae el053d	2/11/2015 18:00:00	Ef On Sv Wn Wz Zc	3600
raks13af	18/11/2015 10:00:00	On Wn Wz	3600
raks13ag	19/11/2015 09:00:00	Ef On Wn Wz	3600
raks13aj	6/12/2015 10:00:00	Ef On Wn Wz	2700
raks13ak	8/12/2015 20:00:00	Ef On Wn Wz	3600
raks13an el053e	28/05/2016 11:00:00	Ef On Sv Wn Wz Zc	3600
raks13ao el053f	29/05/2016 12:00:00	Ef On Sv Wn Wz Zc	3600
raks13aq el053h	14/06/2016 19:00:00	Ef On Sv Wn Wz Zc	1800
raks17ac	11/07/2016 07:39:00	Ma Wn Wz	1860
raks17ad	11/07/2016 10:20:00	Ma Wn Wz	1200
raks17ae	20/07/2016 01:11:00	Ef Wn	2340
raks17ai	28/07/2016 19:43:00	Pu	2220

Table 4.4: *List of experiments*

exp. no	date	code	telescopes
1	2015-10-24	raks13ab el053a	Ef On Sv Wn Wz Zc
	2015-10-25	raks13ac el053b	Ef On Sv Wn Wz Zc
2	2015-10-31	raks13ad el053c	Ef On Sv Wn Wz Zc
	2015-11-02	raks13ae el053d	Ef On Sv Wn Wz Zc
3	2015-11-18	raks13af	On Wn Wz
	2015-11-19	raks13ag	Ef On Wn Wz
4	2015-12-06	raks13aj	Ef On Wn Wz
	2015-12-08	raks13ak	Ef On Wn Wz
5	2016-05-28	raks13an el053e	Ef On Sv Wz Wn Zc
	2016-05-29	raks13ao el053f	Ef On Sv Wz Wn Zc
	2016-05-29	raks13an el053g	Ef On Sv Wz Wn Zc
6	2016-06-14	raks13aq el053h	Ef On Sv Wz Wn Zc
	2016-06-15	raks13ar el053i	Ef On Sv Wz Wn Zc
	2016-06-15	raks13as el053j	Ef On Sv Wz Wn Zc
7	2016-07-11	raks17ac	Ma Wn Wz
	2016-07-11	raks17ad	Ma Wn Wz
8	2016-07-20	raks17ae	Ef Wn
	2016-07-20	raks17af	Ef Wn
	2016-07-20	raks17ag	Ef Wn
9	2016-07-28	raks17ai	
	2016-07-29	raks17aj	Ef
10	2016-09-29	raks17aw	
	2016-09-29	raks17ay	
	2016-09-30	raks17az	
	2016-09-30	raks17ba	
11	2016-11-14	raks17bb	Ef On Wn Wz
	2016-11-14	raks17bc	Ef On
	2016-11-15	raks17bd	On
	2016-11-16	raks17be	
12	2016-11-24	raks17bf	
	2016-11-24	raks17bg	
	2016-11-25	raks17bh	
	2016-11-26	raks17bi	
13	2016-12-04	raks17bj	Ef On Ys
	2016-12-05	raks17bk	Ef Ys
	2016-12-06	raks17bl	Ef Ys
	2016-12-06	raks17bm	On
14	2016-12-14	raks17bn	Wn Ys
	2016-12-16	raks17bo	Ys
	2016-12-16	raks17bp	Ef Ys
15	2017-03-12	raks17bq	
	2017-03-12	raks17br	Ef Ys
	2017-03-13	raks17bs	Wn Wz
16	2017-03-26	raks17bt	On Ys
	2017-03-29	raks17bu	Ef Wn
	2017-03-29	raks17bv	Ef Wn
17	2017-04-12	raks17bw	Wn Wz Ys
	2017-04-15	raks17bx	
	2017-04-15	raks17by	On Ys
18	2017-04-20	raks17bz	Wn Ys
	2017-04-20	raks17ca	Wn Ys
	2017-04-23	raks17cb	On
	2017-04-23	raks17cc	On
19	2017-08-01	raks19af	Bd Ys Zc
	2017-08-10	raks19ag	Ef Wn Wz
	2017-08-10	raks19ah	Ef Wz
	2017-08-11	raks19aj	Wz
	2017-08-11	raks19ak	
	2017-08-20	raks19al	Ef Ys
	2017-08-20	raks19am	Ef
	2017-08-21	raks19ao	Bd Sv Wn Wz Zc
	2017-08-22	raks19ap	Sv Wn

Table 4.5: *Ground stations coordinates, [7]*

Ground station	Altitude [m]	Latitude [rad]	Longitude [rad]
Ef	416.674	0.88	0.12
On	20	1.002	0.208
Sv	80	1.056	0.520
Wn	611	0.860	0.224
Wz	611	0.858	0.225
Zc	970	0.764	0.725
Ma	536.9	0.709	0.2915
Pu	239.091	0.9568	0.6567

The nominal settings of the a priori covariance matrix are summarized in Table 4.6:

Table 4.6: *A priori covariance set up used in nominal simulations.*

Estimated Parameters	Covariance (a priori)
Position coordinates	$1.7 \times 10^4 [m^2]$
Velocity coordinates	$2.0 \times 10^{-6} [m^2/s^2]$
Radiation pressure coefficients	100
EEP violation parameter	10^{-6}
Pushchino station coordinates	$100 [m^2]$
Biases	$\sigma^2_{\frac{\Delta f_0}{f}}$ ranging from 10^{-14} to 10^{-11}

The nominal simulation settings used for the observations noise belong to the same interval as the a priori frequency offset uncertainties reported in Table 4.6. They consist of 4 logarithmically spaced values for the fractional frequency fluctuations that lie within the range $[10^{-14} - 10^{-11}]$. This enables to study how sensitive is the EEP violation parameter estimation to the measurements uncertainties and the statistical properties of the frequency bias, which are believed to be the limiting factors of the experiment.

In conclusion, an overview of the global simulations architecture is given by Figure 4.1.
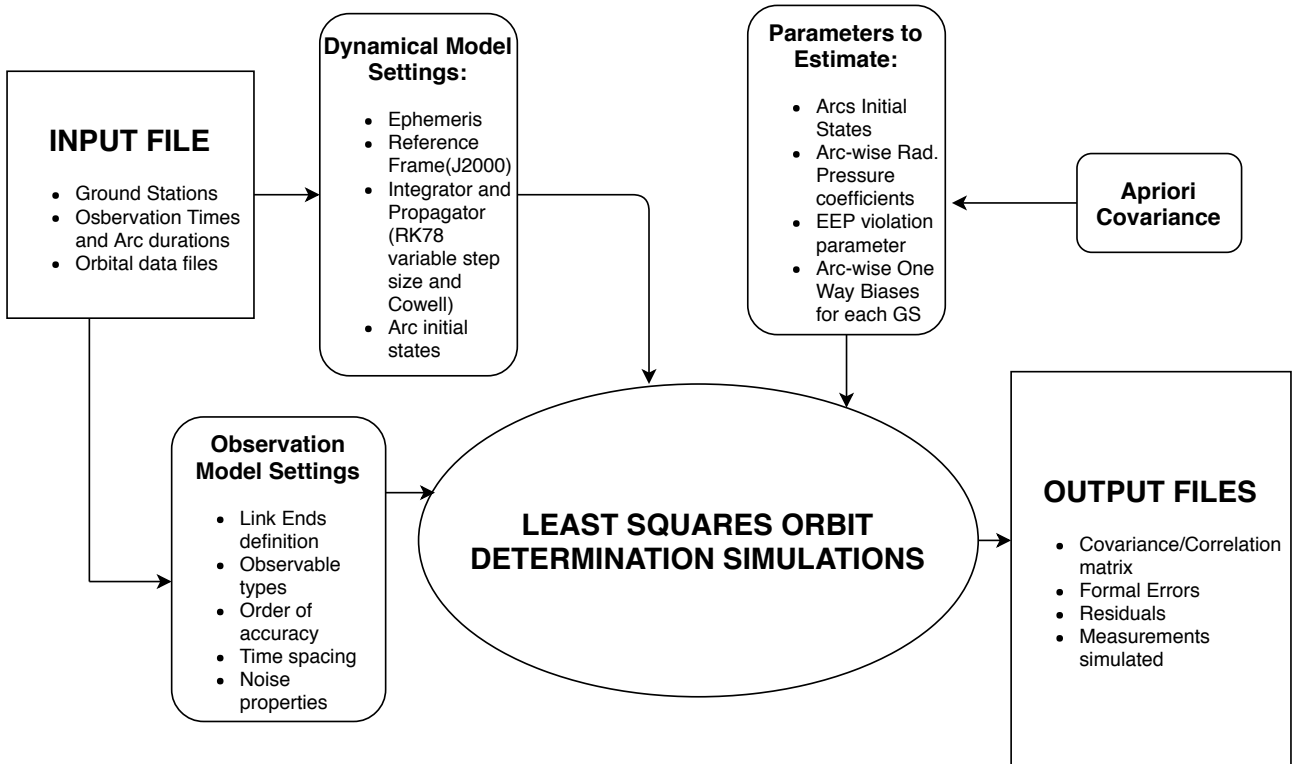
Figure 4.1: *Software architecture for the gravitational redshift experiment simulations study*

4.4   Live RA Doppler measurements

In this section some real Doppler measurements of RadioAstron downlink signal are shown. The observations were Doppler analyzed with the PRIDE tracking method during the internship at the Aalto University in Finland using the software developed by Dr Molera ([27], [28]). The importance of showing real frequency observations is to support and validate the approach adopted for the simulations. Some of the assumptions were formulated, in fact, basing them on the results obtained with the real data processing.

The frequency detections acquired during the experiment el053a by Onsala ground station (which is among the Gravitational Redshift Experiments list in Table 4.4) are shown in the following figure.
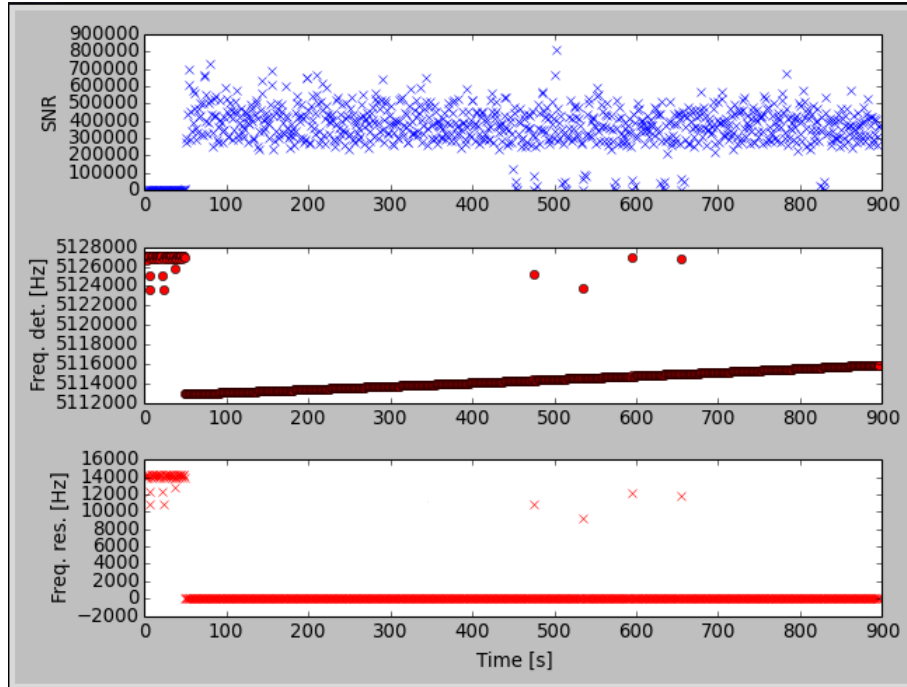
Figure 4.2: *Experiment el053a, On station. First Doppler estimation with PRIDE tracking algorithm.*

As seen from Figure 4.2, during the observation time interval the SNR drops down to zero both at the beginning (approximately the first 50 seconds) and sometimes in the middle (between 400 and 700 seconds). This results in visible discontinuities in the frequency detections plot. The last graph shows the frequency residuals obtained after the Doppler effect compensation which is done through a polynomial fit of the frequency detections. The final results after the last phase stop of the signal are shown in Table 4.7.

Table 4.7: *Experiment el053a (24 October 2015). Details of the experiment and description of the signal's phase stop with PRIDE tracking algorithm.*

Station	Scan #	Freq. Interval [MHz]	Time interval [s]	Phase rms [rad]	Doppler noise [Hz]
Ef	1	[5.0 , 5.2]	[50 , 450]	4.8495291594	0.0176867118957
On	1	[5.0 , 5.2]	[50 , 450]	0.212571748348	0.00243326351357
Sv	1	[5.0 , 5.2]	[50 , 450]	0.204802948366	0.0039171536214
Zc	1	[5.0 , 5.2]	[50 , 450]	1.22684017918	0.0340884960954

The values of the Doppler noise correspond to a fractional frequency fluctuation of the order of $10^{-12}-10^{-13}$ (the RA transmitter is at 8.4 GHz), which is in accordance with the chosen observations noise values for the simulations study, reported in section 4.3.

Moreover, an important conclusion achieved with the real data processing is about the properties of the Doppler noise. This analysis was done by means of an averaging time study. An example is reported in Figure 4.3, where the data is related to the experiment coded rk17ab.
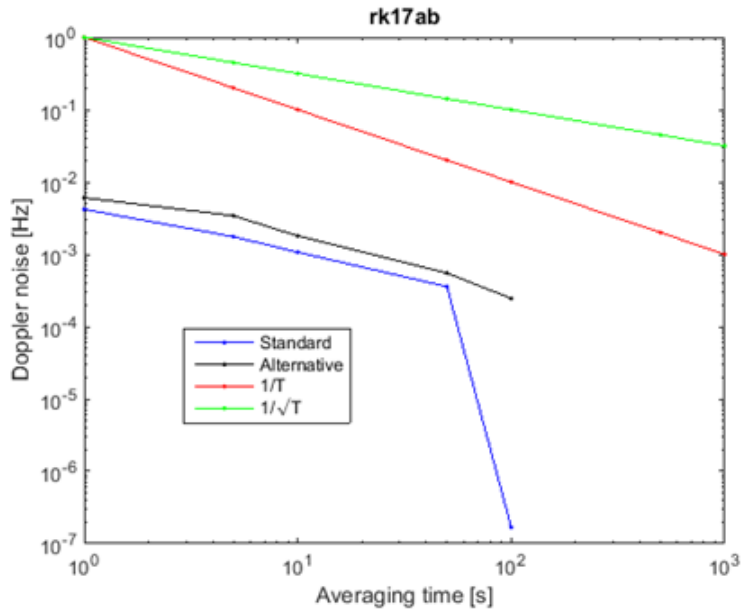
Figure 4.3: *Doppler noise as a function of averaging time in the experiment rk17ab*

As seen from the plot, the Doppler noise (both blue and black lines) follows the $1/\sqrt{T}$ behaviour. The difference between the "standard" and the "alternative" approaches is simply in the procedure adopted to compute the noise. The alternative approach works better with higher averaging times when the standard algorithm crashes.

The outcome of the averaging time study suggests that the RadioAstron downlink signal noise has similar properties to the Gaussian noise. Therefore the assumption made in the simulations study can be considered realistic.

4.5   Verification and Validation

4.5.1   Dynamical model verification

The first step towards the verification of the simulation study was to check that the dynamical model implemented in the software was realistic enough to describe RadioAstron trajectory. To this extent, some orbital data provided by Dr Mikhail Zakhvatkin (Keldysh Institute of Applied Mathematics, Moscow, Russia) were used for comparison purposes and to perform a test of the least squares algorithm of the Tudat. The provided data consisted of state vector parameters (position and velocity) relative to the month of March 2016, hourly spaced in time. Given the software these observations as input, the orbit determination tool was run. The following figures show the residuals between the computed orbit and the given input data. The orbit determination process was performed for each of the 4 weeks of the month.
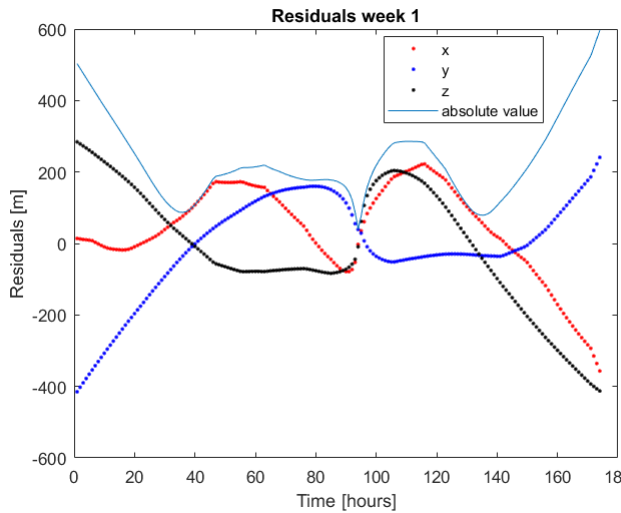
Figure 4.4: *Residuals between Tudat orbit propagation and reference RA orbital data during the first week of March 2016*
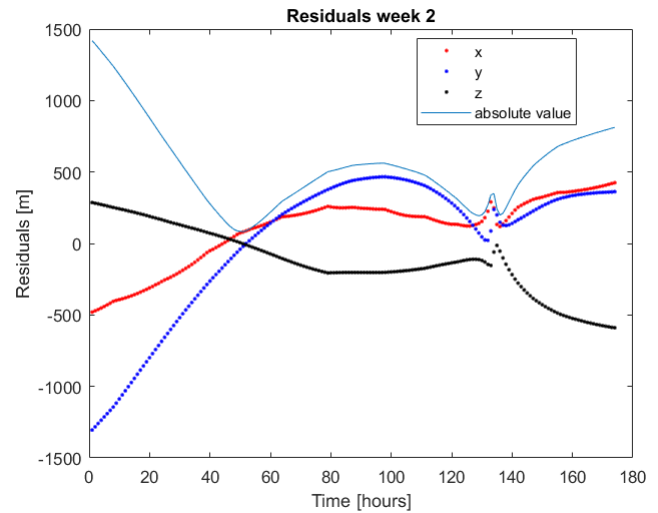
Figure 4.5: *Residuals between Tudat orbit propagation and reference RA orbital data during the second week of March 2016*
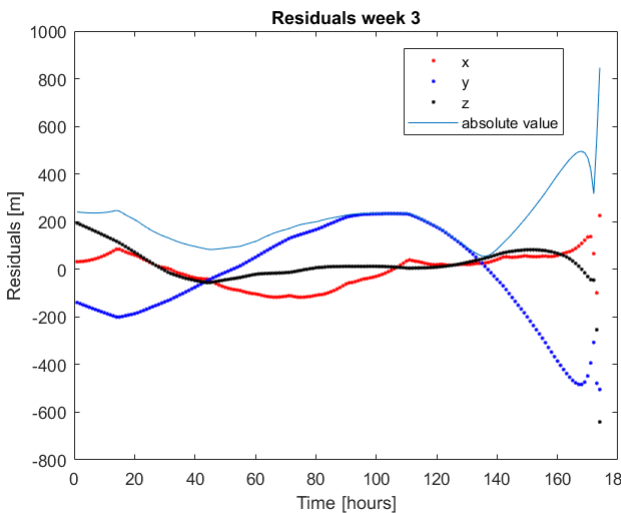
Figure 4.6: *Residuals between Tudat orbit propagation and reference RA orbital data during the third week of March 2016*
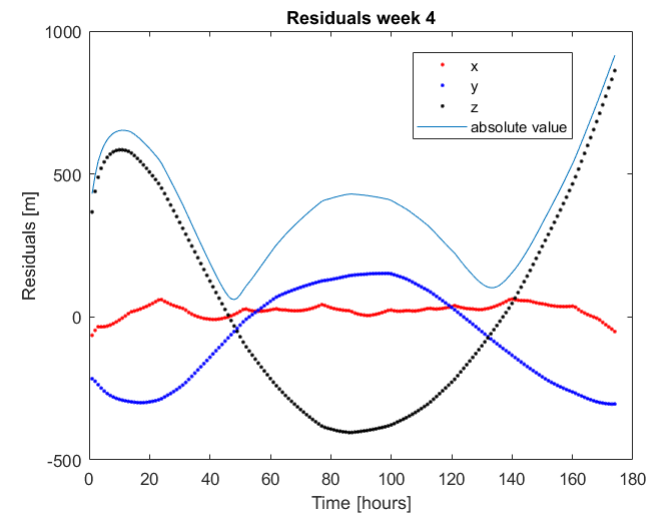
Figure 4.7: *Residuals between Tudat orbit propagation and reference RA orbital data during the fourth week of March 2016*

As seen from the plots, the absolute values of the residuals have a mean corresponding to roughly 200 meters for every week and their standard deviation is not extremely large. Although the curves do not exactly follow the same path in the four different time intervals, in every case their distribution reminds of a quadratic form, which is in particular more pronounced in a Figure 4.5 and Figure 4.7. This is a very positive indicator that the fit provided by the software is good: it means, in fact, that the constant and linear terms are well compensated by the orbital solution achieved by the algorithm. Finally, considering that, according to the RadioAstron Navigation support team, there is an uncertainty of about 200 meters in the satellite position, the obtained results can be defined reasonable.

In this simple orbit determination simulation, the estimated parameters (per week) were the initial position, velocity and radiation pressure coefficient (the cannonball model is adopted, as described in section 3.2). The estimated solar radiation pressure coefficients are significantly different for every week (differences are up to 0.5). This was indeed an expected result because the effect of the light pressure on RadioAstron varies with time according to the spacecraft attitude with respect to the Sun. Therefore, the cannonball model does not well represent reality since the resulting acceleration on the spacecraft is assumed to be always along the Sun's direction while this is not true due to the particular shape of the satellite. Moreover, estimating the radiation pressure coefficient for shorter or longer time intervals than one week brings even larger differences that can be up to a factor of 2. Given the outcome of this preliminary study two important assumptions were made in the

nominal simulations settings (see section 4.2). First, the radiation pressure coefficients were estimated arc-wise (each arc/experiment is roughly one hour long) and, second, their a priori uncertainty was set to the very large value of 10.

4.5.2 Implementation of the EEP violation parameter estimation

Once tested the basic functionality of the least squares algorithm in estimating the spacecraft state vector with realistic results, the implementation of the EEP violation parameter estimation was the next important step to be verified. To do so, it was necessary to generate Doppler observables in the orbit determination process (especially one way data, since the two way link measurements do not depend on ε, being the gravitational redshift cancelled out) and check if the partial derivatives with respect to ε were correct. The analytical expression of $\frac{\partial \frac{\Delta f}{f}}{\partial \varepsilon}$ is obtained starting from Equation 3.1 after including ε in it. Since the EEP violation parameter affects the proper time rate, Equation 3.4 shall be, in fact, rewritten as:

$$\frac{d\tau}{dt} \approx 1 - \frac{1}{c^2}\left(\frac{v^2}{2} + U(1+\varepsilon)\right) \tag{4.1}$$

therefore:

$$\frac{\partial \frac{\Delta f}{f}}{\partial \varepsilon} = \frac{\partial \left(\frac{f_A - f_B}{f_B}\right)}{\partial \varepsilon} = \frac{\partial \left(\frac{f_A}{f_B}\right)}{\partial \varepsilon} = \frac{\partial}{\partial \varepsilon}\left[\frac{1 - \frac{1}{c^2}\left(\frac{v_B^2}{2} + U_B(1+\varepsilon)\right)}{1 - \frac{1}{c^2}\left(\frac{v_A^2}{2} + U_A(1+\varepsilon)\right)}\frac{dt_B}{dt_A}\right] \tag{4.2}$$

where the coordinate time transfer term has not been fully developed here as in section 3.1, being not a function of ε.

Working out Equation 4.2, leaving for now $\frac{dt_B}{dt_A}$ apart, brings:

$$\frac{\partial}{\partial \varepsilon}\left[\frac{1 - \frac{1}{c^2}\left(\frac{v_B^2}{2} + U_B(1+\varepsilon)\right)}{1 - \frac{1}{c^2}\left(\frac{v_A^2}{2} + U_A(1+\varepsilon)\right)}\right] = \frac{-\frac{U_B}{c^2}\left[1 - \frac{1}{c^2}\left(\frac{v_B^2}{2} + U_B(1+\varepsilon)\right)\right] + \frac{U_A}{c^2}\left[1 - \frac{1}{c^2}\left(\frac{v_A^2}{2} + U_A(1+\varepsilon)\right)\right]}{1 - \frac{1}{c^2}\left(\frac{v_A^2}{2} + U_A(1+\varepsilon)\right)^2} \tag{4.3}$$

which, after neglecting the terms of order $\frac{1}{c^4}$ and making use of Equation 3.11 to express $\frac{dt_B}{dt_A}$ up to the first order in $\frac{1}{c^2}$, becomes:

$$\frac{\partial \frac{\Delta f}{f}}{\partial \varepsilon} \approx \frac{\Delta U}{c^2}\left(1 - \frac{\dot{D}}{c}\right) \tag{4.4}$$

where $\dot{D}$ is defined in section 3.1 and represents the radial velocity, while ΔU is the gravitational potential difference.

Equation 4.4 enables then to verify that the partial derivatives computed by the algorithm are correct. The comparison has been made with the data generated during an orbit determination simulation in which ε is estimated and the following plot reports the result:
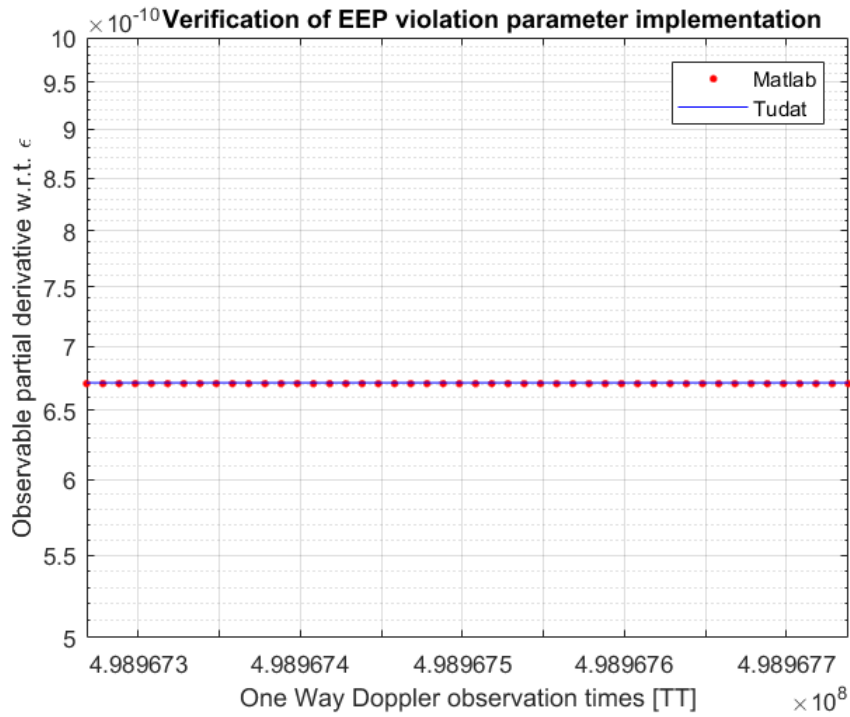
Figure 4.8: *Comparison between the partial derivatives of one way Doppler observables w.r.t. ε computed with Equation 4.4 (red) and the Tudat software (blue)*

Figure 4.8 is related to the one way Doppler observations simulated during the first time arc of the list shown in Table 4.4. The difference between the red and blue values is of the order of 10^{-13} which is very small considering the y-axis scale. This might depend on the different models adopted in the two cases for the Earth gravitational potential as well as on slightly different μ values. Equation 4.4 is, in fact, implemented in Matlab where U is described with the simple central gravity model, while the Tudat settings for the Earth are much more detailed as shown in Table 4.1.

4.5.3 Verification of Noise implementation

The noise settings adopted during the simulations have been verified by checking the distribution of the residuals obtained after the least squares algorithm application. The statistical distribution of the residuals agrees with the chosen noise settings in the software. This is shown in Figure 4.9:
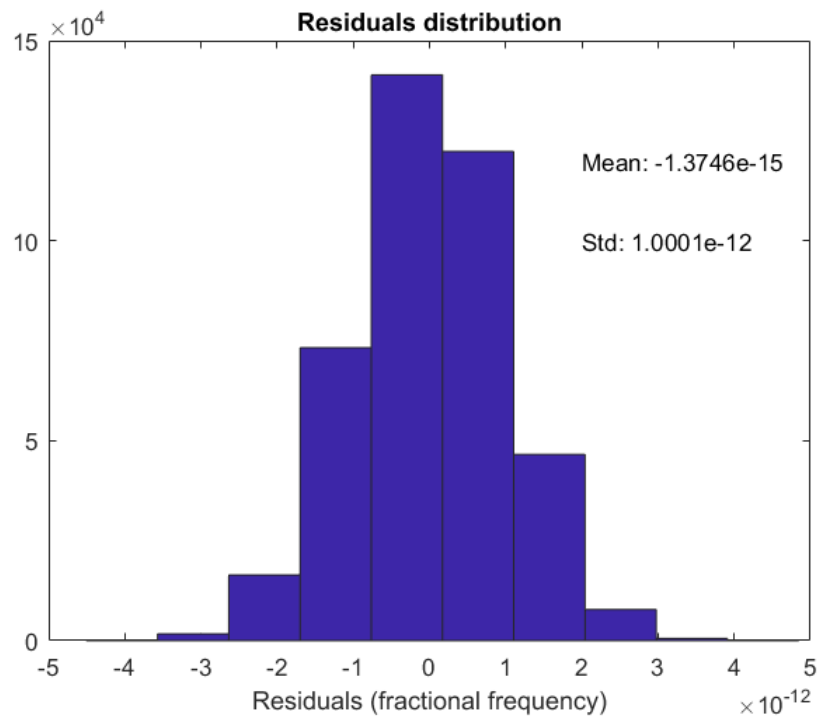
Figure 4.9: *Residuals distribution obtained applying settings of white Gaussian noise with standard deviation of 10^{-12} in terms of fractional frequency fluctuations.*

The residuals resemble the Gaussian distribution so the noise settings are verified.

4.5.4 Validation of correlations between EEP violation parameter and spacecraft state vector

A very important validation of the results obtained about the correlations of the EEP violation parameter with RadioAstron state vector in section 5, is provided by the analysis performed by Dr Mikhail Zakhvatkin by means of a covariance analysis over a one month orbit reconstruction in which ε is estimated. The correlations result are reported in Figure 4.10
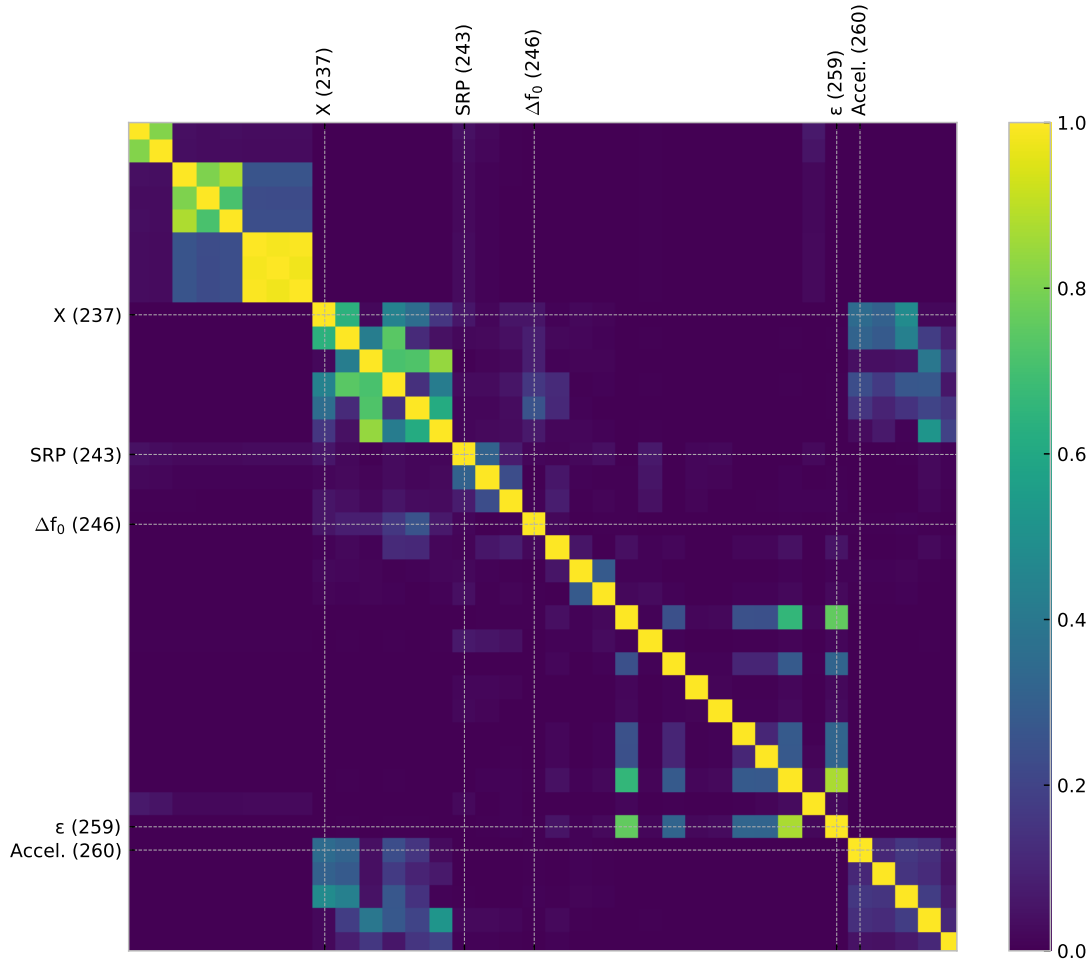
Figure 4.10: *Correlations obtained with a covariance analysis performed by Dr Mikhail Zakhvatkin through a one month RadioAstron orbit reconstruction.*

The correlations of ε with the spacecraft state vector parameters are almost zero in accordance with the results shown in section 5.1. The correlations of the H-maser biases with the EEP violation parameter are, on the other hand, different from the ones obtained with the present simulation study. However, the a priori assumptions about the frequency offsets are quite different in the two analysis. The correlations reported in Figure 4.10 are obtained, in fact, by assuming that the H-maser biases are constant throughout a period of $2-3$ days while in the results shown in section 5.1 the biases are constant throughout one hour time intervals and change according to both stations and time arcs.

Chapter 5

Results

This chapter provides the results of the simulations study whose concept is described in chapter 4. The EEP violation parameter formal error and the correlations between the estimated parameters are reported in section 5.1. In section 5.2, the consider covariance analysis related to Pushchino coordinates is shown and section 5.3 provides the physical interpretation of all the obtained simulations results.

5.1 EEP violation parameter formal error and correlations

The main simulation results regarding the ε formal error, obtained by varying both noise and biases statistical properties applying the settings described in Table 4.6, are shown in Figure 5.1 and Figure 5.2. The specific values are reported in Table 5.1.
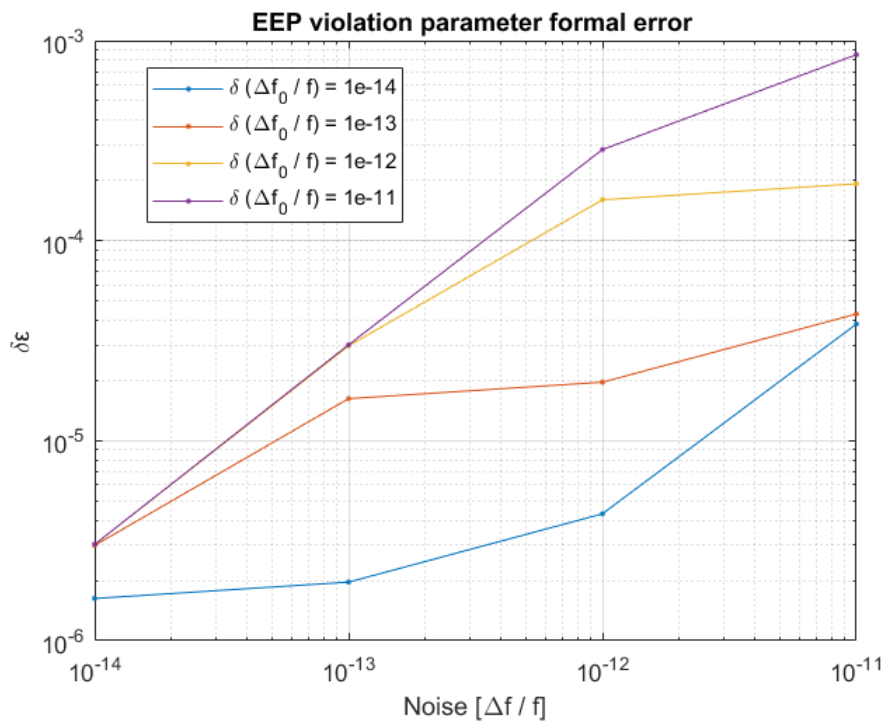
Figure 5.1: *ε formal error as a function of noise and frequency offset a priori uncertainty*
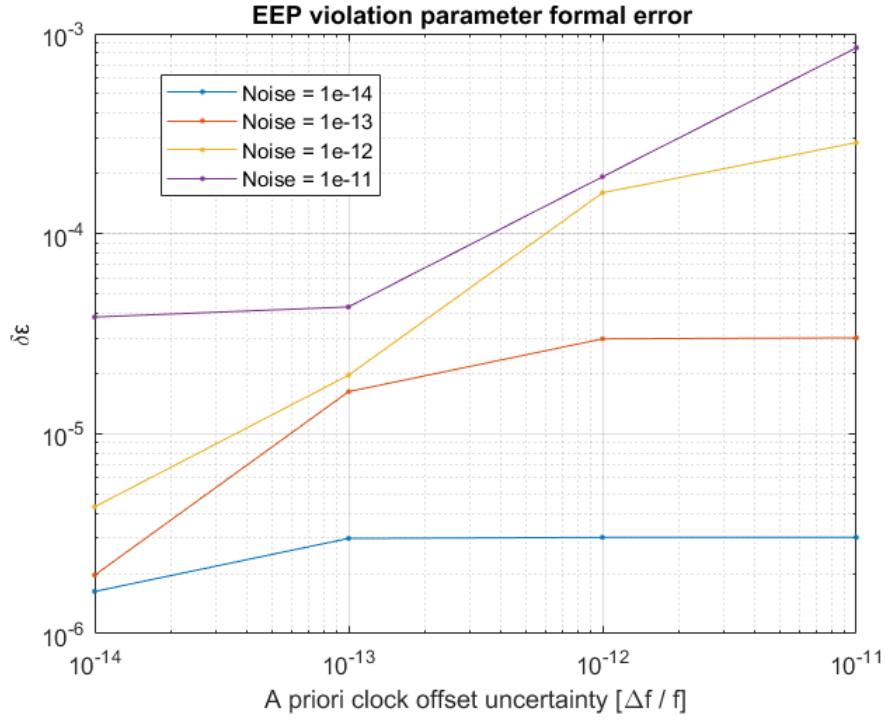
Figure 5.2: *ε formal error as a function of noise and frequency offset a priori uncertainty*

Table 5.1: *EEP violation parameter formal error obtained with different noise and a priori bias uncertainty settings in terms of fractional frequency fluctuations*

Bias\Noise	10^{-14}	10^{-13}	10^{-12}	10^{-11}
10^{-14}	1.6255×10^{-6}	1.9623×10^{-6}	4.3079×10^{-6}	3.8298×10^{-5}
10^{-13}	2.9937×10^{-6}	1.6221×10^{-5}	1.9608×10^{-5}	4.3020×10^{-5}
10^{-12}	3.0302×10^{-6}	2.9786×10^{-5}	1.6013×10^{-4}	1.924×10^{-4}
10^{-11}	3.0306×10^{-6}	3.0146×10^{-5}	2.855×10^{-4}	8.512×10^{-4}

The global visualization of the computed correlations between the whole list of estimated parameters is reported in Figure 5.3. The picture was obtained with noise and a priori clock offsets uncertainty of 10^{-12} in terms of fractional frequency fluctuations. The order of the parameters is the following:

- Initial states of each arc (parameter indexes from 1 to 90 in the correlation figures)
- EEP violation parameter (represented as ε and corresponding to index 91)
- Arc-wise radiation pressure coefficients (92 to 106, represented with C_r)
- Ground station coordinates of PU (107 to 109, represented as Pu)
- Arc-wise one way biases (110 until the end)
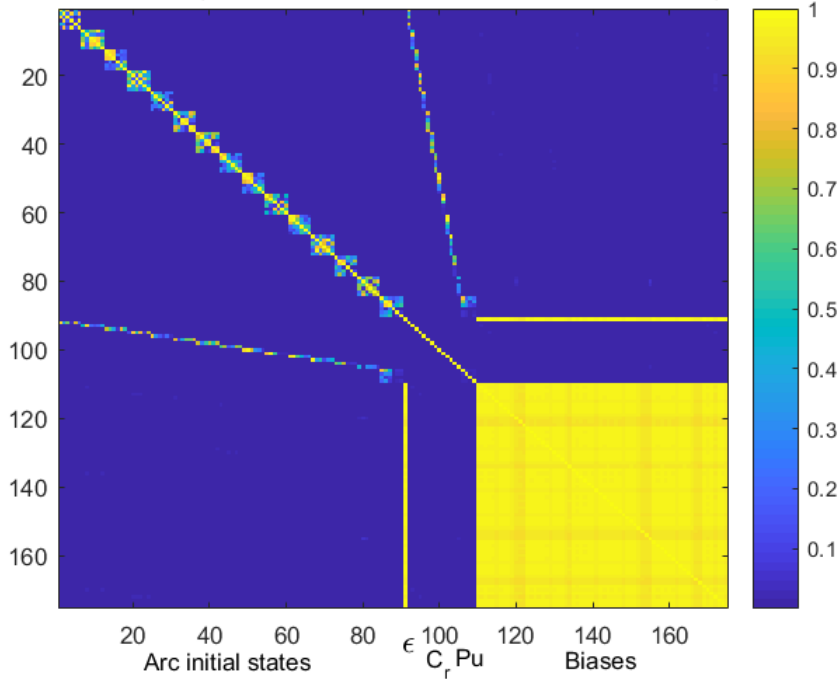
Figure 5.3: *Correlations of the estimated parameters. Results obtained with fractional frequency noise and clock offsets uncertainties set to $\frac{\Delta f}{f} = 10^{-12}$*

The correlations of the EEP violation parameter with the spacecraft state vector and with the coordinates of Pushchino tracking station are negligible (being almost zero) also in all the other simulated scenarios (different noise and biases settings). On the other hand, the correlations of ε with the absolute biases in one way observations experience significant changes depending on the noise and H-maser offsets statistical properties. The situation is described in Figure 5.4 and Figure 5.5, where the mean correlation values reported on the y-axis correspond to the average correlation of ε with the biases. The specific values are provided in Table 5.2
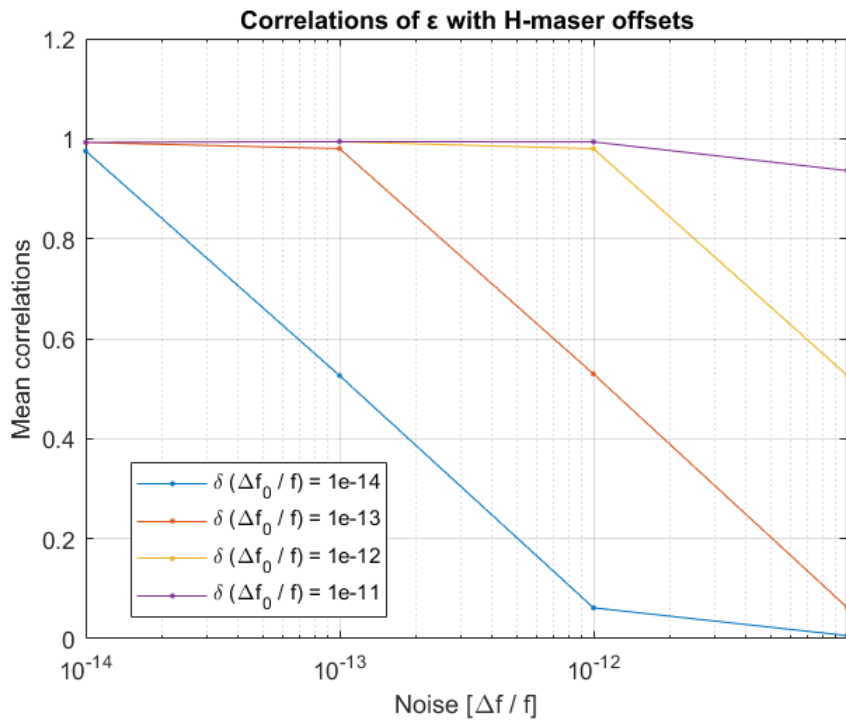
Figure 5.4: *ε formal error as a function of noise and frequency offset a priori uncertainty*
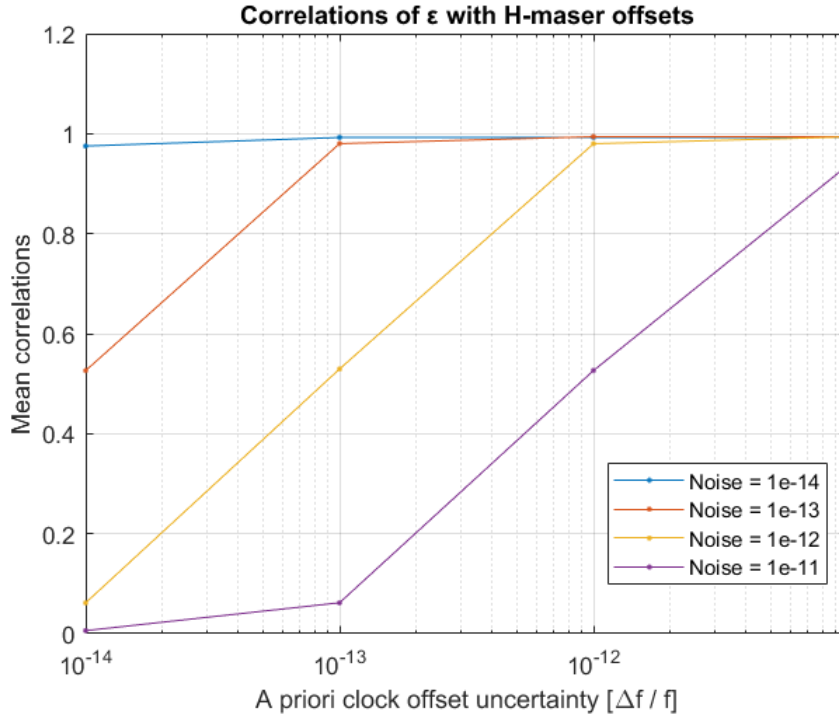
Figure 5.5: *ε formal error as a function of noise and frequency offset a priori uncertainty*

Table 5.2: *Mean correlation values of EEP violation parameter with one way frequency biases with different noise and a priori bias uncertainty settings in terms of fractional frequency fluctuations*

Bias\Noise	10^{-14}	10^{-13}	10^{-12}	10^{-11}
10^{-14}	0.975	0.526	0.0617	0.00612
10^{-13}	0.992	0.980	0.529	0.0618
10^{-12}	$0,993$	0.994	0.980	0.526
10^{-11}	0.993	0.994	0.994	0.936

A few simulation tests with noise values below 10^{-14} have shown an exceptional case of decorrelation between one single bias and ε, detected during the 15th time arc. Although the mean correlation of ε with the biases remains still very high, this exceptional case consists of a correlation coefficient of 0.4 against the other values ranging in the interval $0.84 - 0.99$. This phenomenon is shown in Figure 5.6 and will be discussed in part in section 5.3.
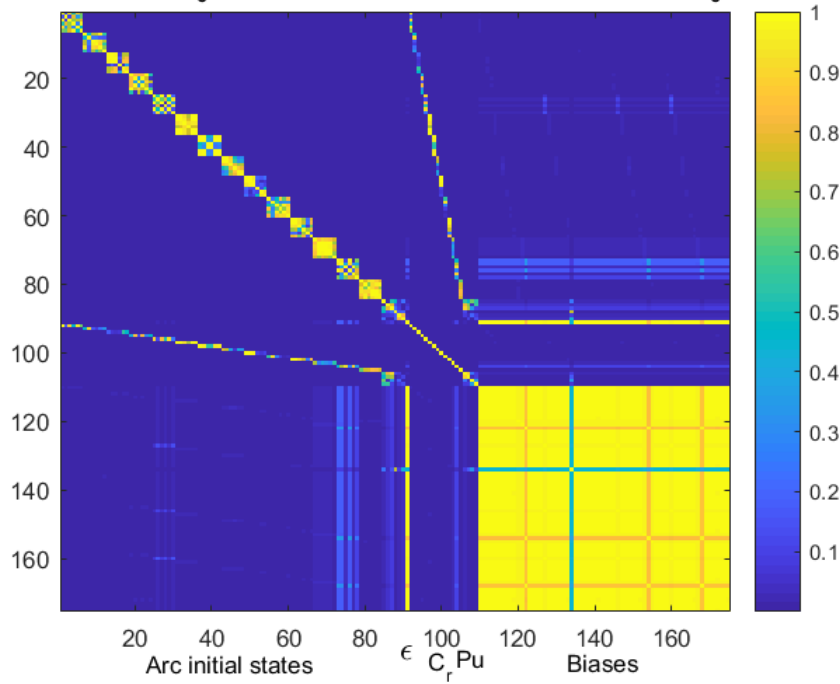
Figure 5.6: *Correlations of the estimated parameters. Results obtained with fractional frequency noise set to $\frac{\Delta f}{f} = 10^{-15}$ and clock bias uncertainty 10^{-12}*

5.2 Consider covariance study on Pushchino tracking station position accuracy

Estimating the station coordinates in the simulations might affect the reliability of its correlations with the EEP violation parameter: this was the main doubt raised by the research group. Therefore, since this issue is extremely important for interpretation of experimental data, a further investigation was made through a consider covariance study. As discussed in section 3.4.1, this analysis consists of evaluating the impact of the a priori uncertainty of non estimated parameters (in the present case Pushchino station coordinates) on the final solution accuracy. More specifically, for the current project study, the impact on the correlations is the most important result. Figure 5.7 shows the new computed correlations matrix in which the tracking station cartesian coordinates are identified by the last three parameters. Their a priori uncertainty values (σ) are set to 10 m while random noise and bias a priori standard deviations are both set to 10^{-12} in terms of fractional frequency fluctuations.
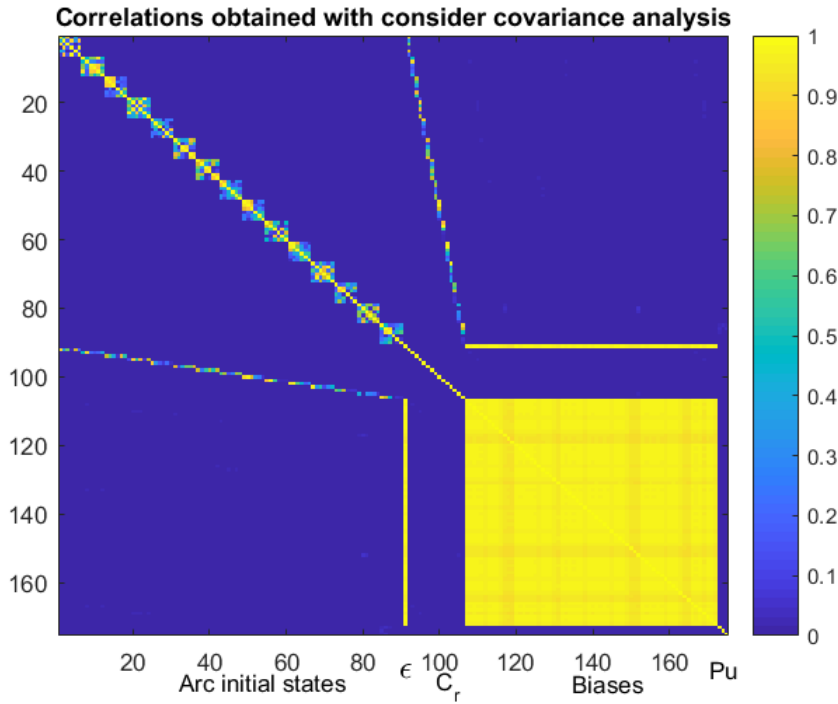
Figure 5.7: *Consider covariance analysis. Pushchino station coordinates are the last three parameters while ε is parameter 91. Fractional frequency of noise and bias uncertainties set to 10^{-12}.*

As seen in the figure, the correlations with the EEP violation parameter have not changed respect to the previous cases. Moreover the EEP violation parameter formal error is $1.6013e-04$ which does not change respect to the case in which Pushchino coordinates are estimated. This result shows that the ground station position uncertainty is harmless even if the station coordinates are not estimated, following the more realistic approach of the consider covariance analysis.

5.3 Interpretation of the results

The obtained ε formal error as a function of the observations noise and clock offset statistics, along with the correlations between the estimated parameters provide a good answer to the main research questions given in the introduction. The ε formal error represents the accuracy of the gravitational redshift experiment and the correlation images give a clear idea of how the parameters uncertainties are related to each other.

5.3.1 EEP violation parameter formal error

The two simulated scenarios described in Figure 5.1 and Figure 5.2, in which the observations noise and the a priori covariance of the H-masers offsets vary within the same range of values (expressed as fractional frequency fluctuation), are similar but present a few differences. In general, the ε formal error is influenced by both noise and clock uncertainty when one setting is fixed respect to the other. However, as expected, noise has a greater impact on the experiment accuracy because this setting directly affects the measurements quality respect to the a priori knowledge of the clock uncertainty. It is clear, for instance, that a noise level of 10^{-11} sets a limit to the achievable experiment accuracy as shown in Figure 5.2. All the other a priori constraints given to the satellite state vector uncertainty, radiation pressure coefficients and Pushchino coordinates do not influence ε formal error in a significant way as noise and frequency bias do (they are, in fact, not correlated with ε as shown in Figure 5.3). According to the expectations of the real experiment ([4]), the formal error obtained with the simulations lies in a range of realistic values (they are a bit optimistic though because of the simplified simulations assumptions). Further considerations about the achievable experiment accuracy are given in section 5.3.5.

5.3.2 Correlation between satellite initial states and EEP violation parameter

An impressive result of the analysis is, indeed, the fact that ε is poorly correlated with the satellite state vector parameters. However this result has a physical explanation supported by the structure of Equation 3.15. The temporal signature of the initial states and ε on the frequency observable is, in fact, very different. Changes in the state vector parameters are reflected into significant variations of the first order Doppler which affects the total $\Delta f_{1w}/f$ in a very different and much larger way respect to the changes in the gravitational redshift effect due to ε variations. The different sensitivities of the frequency observable w.r.t. the state vector and the EEP violation parameter are shown in Figure 5.8 where the partial derivatives w.r.t. the satellite x initial position of the first arc and ε are plotted as a function of the observation times:
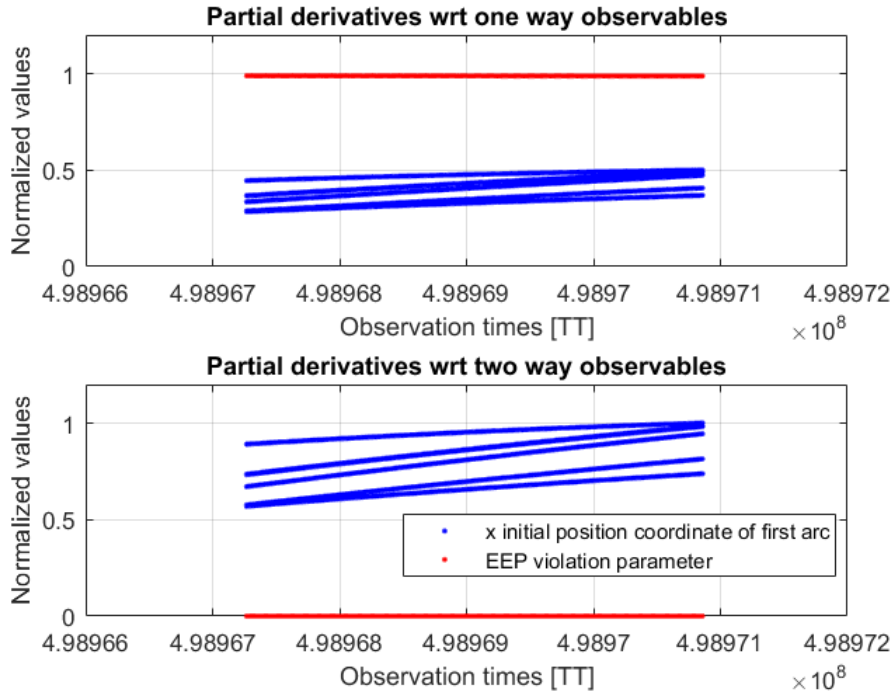
Figure 5.8: *Partial derivatives of observables w.r.t. the EEP violation parameter (red) and x initial position coordinate of the first arc (blue). The different curves of the same color are due both to the different ground stations involved in the observations and the different Doppler observables (one and two way).*

As seen in Figure 5.8, the behaviour of the partial derivatives w.r.t. the two parameters are different and this is an indicator that they are not correlated. As expected, the ε partial derivatives in the second subplot (two way observables) are zero since the two way Doppler measurements are not a function of the EEP violation parameter, being the gravitational redshift term cancelled out. Moreover, as an additional verification step, the derivatives w.r.t. the x initial position coordinate, are almost doubled in the second half of the plot and this is perfectly in accordance with Equation 3.16 because in the two way measurements some of the Doppler terms are actually twice the one way contributions. Actually the combination of one and two way data improves the decorrelation process because of the additional two way observations which are sensitive only to the state vector. The first subplot of Figure 5.8 (one way observables) gives an indication of the different slopes of the red and blue curves. Figure 5.9 provides a zoom into the derivative w.r.t. ε showing that it has a very small negative slope:
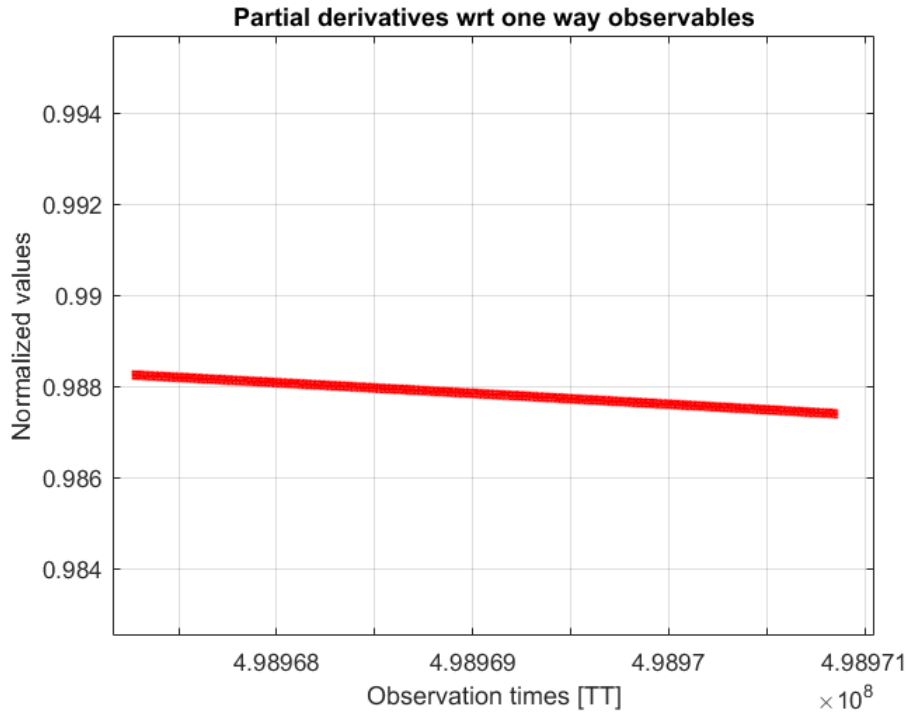
Figure 5.9: *Partial derivatives of one way observables w.r.t. the EEP violation parameter (red). Zoom into the curve.*

The extremely small slope of the red line suggests that the satellite is far from perigee and therefore the gravitational potential has a very small variation within an observation time of one hour, given the characteristics of RadioAstron's orbit (see section 1.2). This is confirmed by the plot of the spacecraft distance from Earth as a function of the observation times, together with the partial derivatives w.r.t. the EEP violation parameter, shown in Figure 5.10:
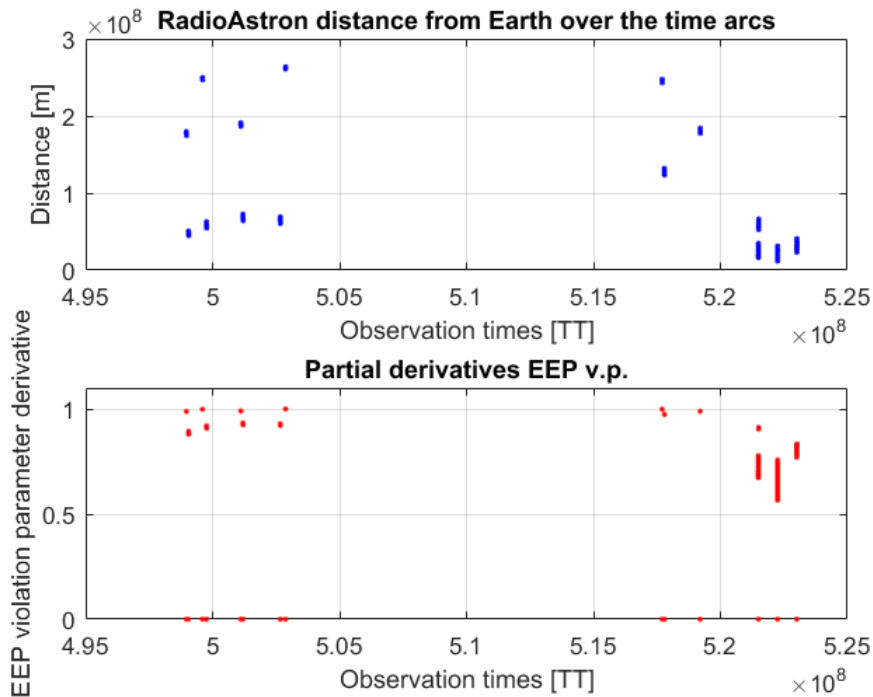
Figure 5.10: *RadioAstron distance and partial derivatives wrt the EEP violation parameter as a function of the observation times.*

It is visible that the derivatives w.r.t. ε experience strong changes during the last arcs. The physical explanation

of this phenomenon is that, based on the time arc of the Doppler observations, the satellite is at different positions along its orbit and, according to its specific orbital dynamics and geometry, it has a different radial velocity. Therefore, according to Equation 4.4, it follows that the derivative behaviour mainly depends on the pattern of the gravitational potential difference. Figure 5.10 shows important aspects which are relevant for the correlations between frequency offsets in one way observations and the EEP violation parameter. This discussion is in section 5.3.4.

Poor correlations of other position and velocity coordinates with ε are explained by a similar discrepancy between their partial derivatives as pictured in Figure 5.8. However, unlike changes in the initial position coordinates, changes in the spacecraft velocity produce definitely larger variations in the frequency observables compared to changes in ε. The reason why quite loose a priori constraints given to the spacecraft state vector (reported in Table 4.6) do not affect the EEP violation parameter accuracy is related to the observations noise level. This affects the weighting matrix in Equation 3.68 in a way that makes measurements more trustworthy compared to the a priori information. It is then important to remember that the state vector parameters are estimated and are not treated as consider parameters.

Finally, as expected, within each arc the state vector parameters (including the radiation pressure coefficient) are cross-correlated but no correlations appear between initial states of different arcs. Although states at different time intervals are related by the orbital dynamics law, the lack of correlations in the present case is a consequence of considering each arc to be statistically independent from the others (see the first assumption stated in section 4.2). This means that the state vector uncertainty is not propagated from an arc to the next one but the a priori covariance matrix is the same at the beginning of every time interval considered for the orbit determination.

5.3.3 Correlation between Pu coordinates and EEP violation parameter

Another important result is that the correlations of ε with Pushchino ground station coordinates are very low. This means that the current uncertainty on the geodetic position of the tracking station does not have a significant influence on the experiment measurement accuracy. This is confirmed by the partial derivatives of one and two way frequency observables w.r.t. the parameters:
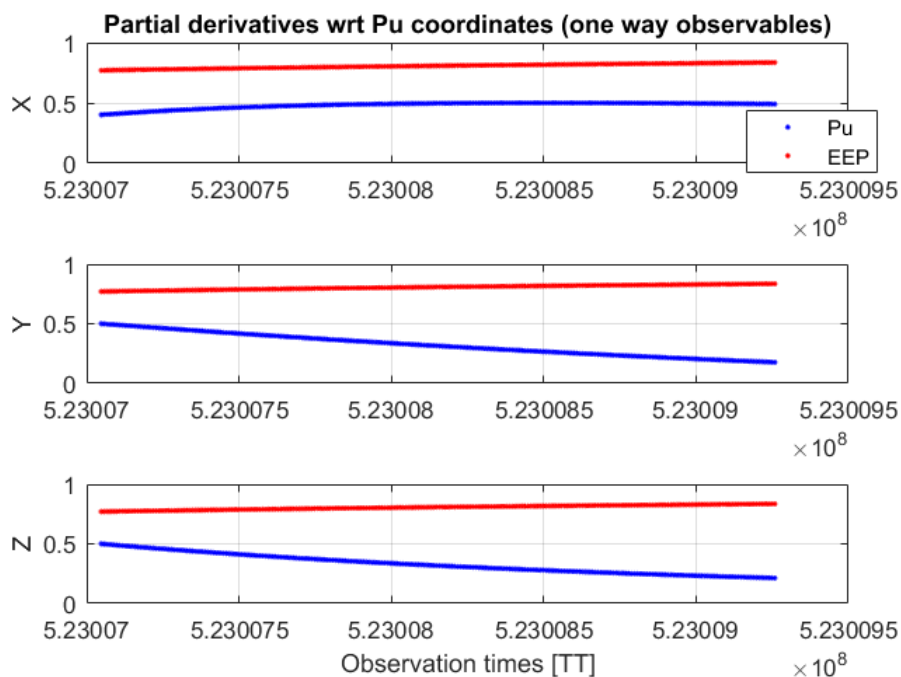
Figure 5.11: *Partial derivatives w.r.t. Pu station coordinates and EEP violation parameter (one way observables).*
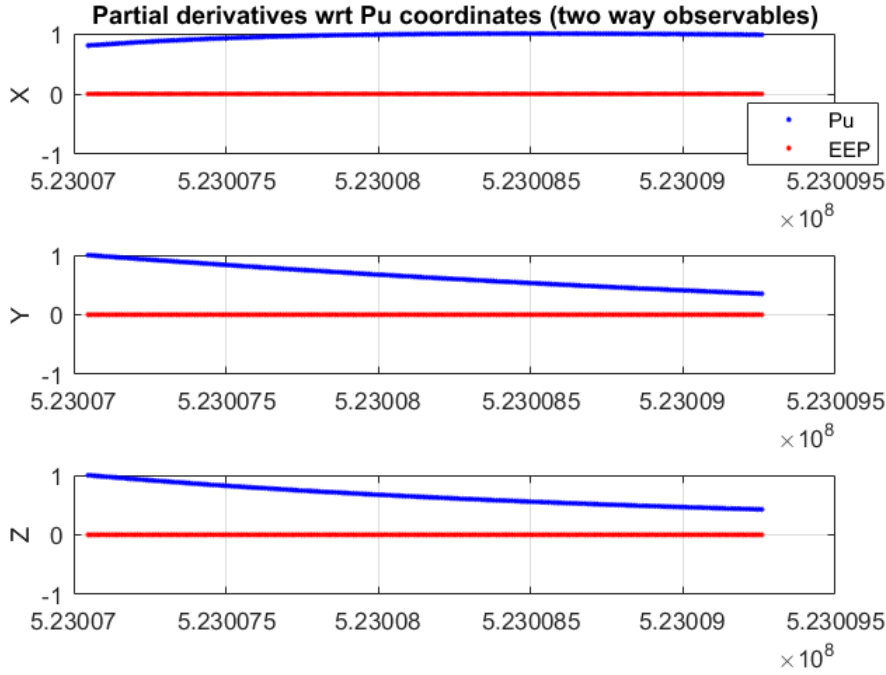
Figure 5.12: *Partial derivatives w.r.t. Pu station coordinates and EEP violation parameter (two way observables).*

As shown in Figure 5.11 and Figure 5.12, the temporal signature of the TS coordinates has a pronounced curvature respect to the ε one. Changes in ε affect the frequency observations in a larger and different way than changes in Pushchino coordinates. Their different behaviour agrees with the low correlation numbers. The formal error of the EEP violation parameter, moreover, is not affected by the assumed 10 meters σ of Pu cartesian coordinates even when these are treated as consider parameters, as presented in section 5.2. Figure 5.7 shows that also correlation-wise there are no changes. Given the same results obtained with the two approaches (covariance and consider covariance) it is possible to conclude that, as long as the geodetic Pushchino coordinates uncertainties are smaller or equal than 10 m (GPS capability), they are harmless for the gravitational redshift experiment.

5.3.4 Correlation between EEP violation parameter and clock offsets

The global correlation images presented in section 5 show that the EEP violation parameter and the clock offsets are in general highly correlated and statistically independent from all the other parameters. From a careful observation of Figure 5.4 and Figure 5.5 it emerges that the correlation values between ε and the biases follow a specific criterion: they depend on the ratio between noise and a priori clock offset uncertainty $\left(\frac{\sigma_{noise}}{\delta\frac{\Delta f_0}{f}}\right)$.

The numbers reported in Table 5.2 agree perfectly with this type of dependency with only one exception in the case of noise and $\delta\frac{\Delta f_0}{f} = 10^{-11}$ where the correlation number is not exactly equal to the other terms of the diagonal. However this result might be less reliable due to the matrices higher condition number obtained with those settings. In general, the higher $\frac{\sigma_{noise}}{\delta\frac{\Delta f_0}{f}}$ gets, the lower the correlations become. This phenomenon can be explained with a few considerations about the measurements principle and the a priori assumptions. Generally speaking, the clock offset and ε are two very distinct and independent variables that are not correlated a priori. One is a fundamental physics parameter while the other one is a bias between two oscillators due to environmental conditions. For this reason their a priori covariance matrix is set to be diagonal (a priori cross correlations are assumed to be zero). On the other hand, when performing the experiment, they happen to be correlated. This is due to the measurement principle and its related complications which make it difficult to distinguish the two contributions. Examining Equation 3.15, it can be noticed that the derivatives of the one way observables w.r.t. the absolute bias are equal to 1 and are constant throughout the observations time according to the assumption made in section 4.2. On the other hand, the derivatives w.r.t. the EEP violation parameter, in the majority of time arcs, are characterized by an extremely small slope so it is difficult to appreciate the sensitivity of the frequency observables respect to ε. The correlations between the two parameters become then very high.

However, Figure 5.10 shows that in some cases (last arcs) the partial derivative w.r.t. the EEP violation

parameter is very steep compared to other arcs. Although this might suggest that in these few circumstances there should be a decorrelation between the two parameters (despite the specific noise and a priori constraints), the outcome of a simulation performed considering only those specific time intervals in which the observables are more sensitive to ε (when the derivative is steep) has brought the same high correlation result (mean value of 0.98 maintaining the nominal settings of 10^{-12} for noise and frequency offset uncertainty). Moreover, if the absolute biases and ε are estimated alone, without all the other parameters included in the nominal simulations, their mean correlation value remains the same.

To investigate this phenomenon a synthetic study was performed in Matlab. By means of a synthetic information matrix, whose columns resemble the partial derivatives w.r.t. ε and the bias, the correlations between the two variables were then reproduced. The column related to the bias was simply described by a constant function equal to 1 (as in the nominal simulations), while the other one (resembling ε) was described with different models: linear, quadratic and sinusoidal. In the linear case both the intercept and the slope were changed to see the impact on the correlations. The covariance was computed without weights and a priori information. It turned out that no matter how much the linear model changes, correlations do not get lower 0.88. Moreover, if both the slope and the intercept are very small, the resulting correlation with the constant absolute bias is almost one. In case the partial derivative w.r.t. ε is described by a parabola the correlations get lower than in the linear case but still remain over 0.5. Finally, in the case of a sinusoidal model, as expected, the correlation between the two parameters goes dramatically down, being close to 0. The correlations obtained with the linear model, varying both the intercept and the slope within the realistic values of the nominal simulations, are represented in Figure 5.13:
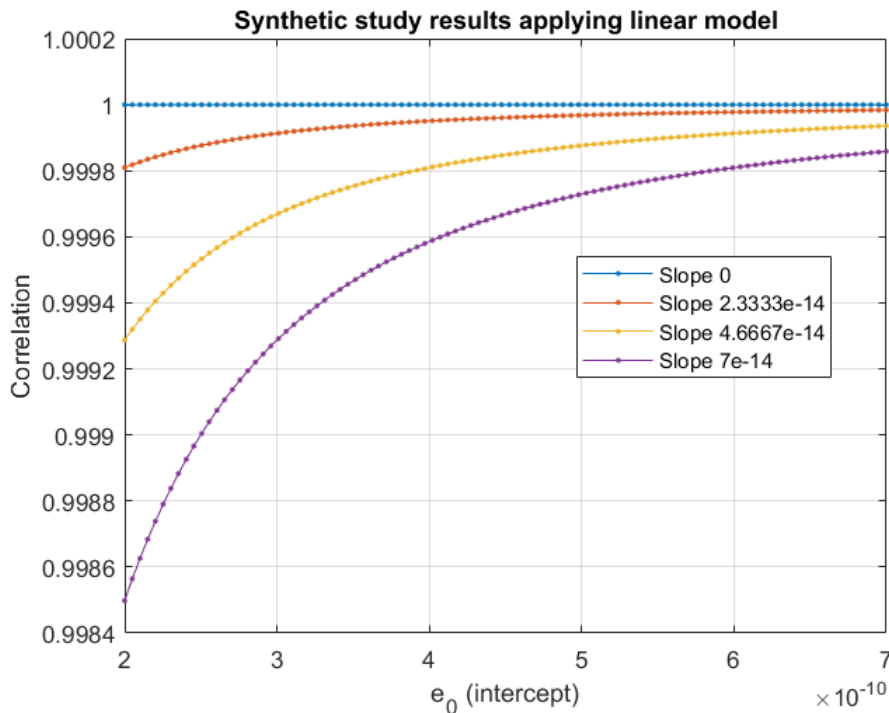
Figure 5.13: *Correlations obtained with the synthetic study by means of a linear model describing the derivative w.r.t. ε*

As seen, correlations are constantly very high. The synthetic study confirms the outcome of the nominal simulations done with the Tudat.

The case of low correlation between clock offset and ε during experiment raks17ai (15th time arc) reported in Figure 5.6 is really surprising. It seems that the decorrelation between the two parameters is related to a combination of circumstances. During that time interval, the x velocity coordinate of the satellite happens to be highly correlated with the bias (correlation coefficient of 0.7, definitely much greater than usual) and, unlike the majority of time intervals, arc number 15 presents a slightly different geometry (the shape of the spacecraft trajectory does not resemble a straight line as it usually happens during one hour time intervals). The derivative w.r.t. ε therefore does not have a linear behaviour but reminds a parabolic one (curvature is very small). This happens also in a couple of previous time intervals but during the last arc the values of $\frac{\partial \frac{\Delta f}{f}}{\partial \varepsilon}_{oneway}$ are higher. The low correlation coefficient of 0.4 between the EEP violation parameter and clock offset could be explained by these coincidences. Although this topic has not been deeply investigated, it points to some further interesting

investigations for possible future gravitational redshift experiments.

To sum up, the correlation issue between ε and Δf_0 arises because of the difficulty in distinguishing their different contributions to the fractional frequency observables. With reference to Equation 3.68, reported below, this is comprised in the term $H^T W H$ which is influenced by noise through the weighting matrix.

$$P_0^{-1} = (P_0^{apr})^{-1} + (H^T W H) \qquad (5.1)$$

The a priori information, on the other hand, does not envisage any correlation between the parameters. Therefore the correlations depend on the ratio between noise and the a priori clock offset uncertainty. When noise is lower than $\delta \frac{\Delta f}{f}$, $H^T W H$ predominates over $(P_0^{apr})^{-1}$ so correlations increase. When noise is greater than the offset uncertainty then $(P_0^{apr})^{-1}$ becomes more relevant and correlations get lower because of its structure.

5.3.5   Final considerations about the experiment achievable accuracy

The real experiment data processing suggests that the fractional frequency noise level is of the order of 10^{-12} ([29]). Data reported in [4] about the Allan deviation of both RadioAstron H-maser and the signal recorded at Effelsberg ground telescope show that, within 3000 seconds averaging time, the clock uncertainty still remains below 10^{-13}. The combination of a 10^{-12} noise with a frequency offset uncertainty of 10^{-13} brings, according to Table 5.1, to an accuracy of 1.9608×10^{-5} on the ε estimation with a mean correlation value with the frequency offsets of 0.53. The ε formal error agrees with the order of magnitude of the expected real experiment accuracy reported in [4] of roughly 2.5×10^{-5}. However, the predicted result of the simulations study is referred to the case in which clock offsets are estimated arc-wise. In reality, differenced measurements between apogee and perigee are considered, as stated in section 1.3. With this approach the constant frequency offset term is cancelled out and only the drift remains. Therefore, in order to have a more realistic error budget, the uncertainty of the clock drift between two gravitational redshift experiment sessions should be known. This value would be a function of time so it would have a different impact according to the time spacing of different gravitational redshift sessions. The implementation of this new approach is described and recommended in section 6.2.

The outcome of the simulations study is quite optimistic for several reasons. Assumptions about the noise profile (which is assumed to be ideally white Gaussian and not time correlated), considering two way observations completely unbiased, not taking into account the interleaving measurement approach and adopting a very simple radiation pressure model to describe the orbital dynamics of RadioAstron are quite strong. The assumption of considering biases that belong to the same link end (spacecraft-ground station) as different independent parameters is also not true because they are a function of time. Therefore they are also a priori correlated. Although this assumption introduces indeed some errors, unlike the others it might actually complicate the estimation problem. If bias differences were estimated instead of absolute values, they would be a function of time and it should be easier to distinguish their temporal signature from ε.

One of the positive aspects, as confirmed by the covariance analysis performed by Dr Mikhail Zakhvatkin with much more accurate models (shortly summarized in section 4.10), is that the simulations study correlations results with respect to the state vector are validated. This means that the simulation concept has been developed correctly. On the other hand, possible unmodelled effects affecting the real frequency fluctuations in terms of noise might represent a dangerous obstacle in reaching $\delta\varepsilon \approx 10^{-5}$.

Chapter 6

Conclusions and recommendations

This chapter provides both a summary of the key points of the project study, along with the results obtained in chapter 5 (this is given in section 6.1), and some future recommendations for further improvements (section 6.2).

6.1 Summary of the results and answers to the research questions

The list of research questions defined in section 1.6 has been discussed and answered throughout the report with the simulations study results. The main subjects to be investigated were the impact of the satellite state vector, the frequency offset (clock contribution), the observations noise and the ground station position (Pushchino) uncertainties on the experiment accuracy (EEP violation parameter estimation), in terms of both formal error and correlations.

The resulting output of the covariance and formal error analysis shows that the satellite state vector uncertainty does not influence the accuracy of the ε estimation, as well as an error in Pushchino tracking station coordinates does not represent a harm. On the other hand, the observations noise together with the frequency offset uncertainty do have a big influence on both the EEP violation parameter formal error and its correlations with biases in one way frequency measurements. In other words, ε turns out to be statistically independent of the spacecraft state uncertainty and all the other parameters included in the simulations, except the arc-wise one way frequency biases (representing the frequency offset due to the H-maser clocks). It is very difficult to distinguish the effect of an absolute bias from the EEP violation parameter since they affect the frequency observables during the experiments in almost the same way. Their correlation depends on the ratio between noise and H-maser offset uncertainty. Therefore, in order to decorrelate them, very low a priori uncertainties need to be set compared to the observations noise level. Moreover, both noise and $\delta\frac{\Delta f_0}{f}$ play a crucial role in determining the accuracy of the ε measurement. In general, noise has a greater influence on $\delta\varepsilon$. However, when either noise or bias uncertainty are fixed to a fractional frequency value of 10^{-12}, variations of one setting respect to the other one yield almost identical ε formal errors (see Figure 5.1 and Figure 5.2, yellow curves). In this specific case, the observations noise and the bias uncertainty are almost interchangeable.

Given the realistic value of measurements noise of 10^{-12} in terms of fractional frequency fluctuations, and an uncertainty of $\frac{\Delta f_0}{f}$ of 10^{-13} (resulting from combining Allan deviations of RadioAstron H-maser and a ground radio telescope for one hour averaging time), the resulting EEP violation parameter accuracy, according to the simulations study, corresponds to an order of magnitude of 1.9608×10^{-5}.

6.2 Recommendations for completion of the RadioAstron gravitational redshift experiment

The first future recommendation concerning the covariance analysis consists in extending it to a more general case in which biases are assumed to be functions of time. In reality, in fact, the frequency offset between H-masers experiences a drift. Therefore, estimating not only the absolute values but also the differences between frequency biases would improve the correlation study. Moreover, since the principle adopted to carry out the real experiment is to measure the gravitational redshift difference and not its absolute value, it would be interesting and more appropriate to see how the EEP violation parameter correlates with the difference between absolute biases. In this case the a priori covariance of the biases differences shall be then differentiated according to the time spacing of the observations, given the time dependency of the H-masers drift. Beforehand, an assumption about the type of variation experienced by the clock bias as a function of time shall be made. The implementation of this new simulation set up is not straightforward and requires changes in the Tudat software.

As already done with Pushshino coordinates, the consider covariance analysis shall be extended to the state vector parameters as well to make sure that their uncertainty does not affect the accuracy of the experiment even if they are not estimated. To implement this, though, the a priori covariance related to the position and velocity of RadioAstron shall be very accurate for each time arc. Adopting a simple diagonal matrix would bring to an unrealistic result since the propagated uncertainty would follow an exponential curve and thus would result in extremely high uncertainty values.

Since the correlations might also have a geometrical nature due to the particular positions of ground stations and spacecraft at the times of the observations, a simulation including all the list of experiments together would be ideal to check if there are any significant changes in the covariance analysis done so far. However, given the analysis performed by Dr Mikhail Zakhvatkin for a very long time interval (a month), nothing is expected to change with respect to the correlations between ε and the state vector parameters. On the other hand, it has been shown that in very particular cases, in combination with low noise, the EEP violation parameter could be decorrelated from the bias, thanks to the favourable characteristics of the spacecraft trajectory during the observations time interval and other circumstances that are not completely clear yet. Investigating this aspect would be great for the design of future gravitational redshift experiments.

Although the covariance analysis provides good support for the real data processing, it does not give an indication of how the true experiment error behaves as a function of the errors affecting the involved parameters. The simulations study as implemented so far, in fact, is not reliable for a true error study because the adopted dynamical model for the spacecraft is not realistic enough and, above all, unmodelled effects in noise might significantly affect the experiment. Therefore, in order to extend the simulations study to the true experiment error, the orbital motion of RadioAstron has to be described with the most accurate model for the radiation pressure force, which represents the main source of uncertainty in the dynamics. Moreover, since the dynamical model will always present some uncertainty, adding process noise to the state vector propagation while implementing the least squares algorithm estimation would be beneficial. With regard to the process noise, however, the most difficult part would be understanding what its appropriate magnitude and time-correlated probability distribution shall be. The first suggestion would be trying different cases and find out how true, formal errors and correlations change according to the chosen process noise matrix.

In conclusion, the application of a least squares algorithm to study the error budget of the experiment represents a very robust mathematical and statistical method. The correlations computed alongside with the parameters estimation add an important value to the formal errors result and give an indication of how reliable is the experiment outcome. Therefore, this rigorous approach of estimating the EEP violation parameter through a statistical orbit determination process might have a great benefit if applied as a technique for the real data processing.

References

[1] N. S. Kardashev, V. V. Khartov, V. V. Abramov, V. Y. Avdeev, A. V. Alakoz, Y. A. Aleksandrov, S. Ananthakrishnan, V. V. Andreyanov, A. S. Andrianov, N. M. Antonov, M. I. Artyukhov, M. Y. Arkhipov, W. Baan, N. G. Babakin, V. E. Babyshkin, N. Bartel', K. G. Belousov, A. A. Belyaev, J. J. Berulis, B. F. Burke, A. V. Biryukov, A. E. Bubnov, M. S. Burgin, G. Busca, A. A. Bykadorov, V. S. Bychkova, V. I. Vasil'kov, K. J. Wellington, I. S. Vinogradov, R. Wietfeldt, P. A. Voitsik, A. S. Gvamichava, I. A. Girin, L. I. Gurvits, R. D. Dagkesamanskii, L. D'Addario, G. Giovannini, D. L. Jauncey, P. E. Dewdney, A. A. D'yakov, V. E. Zharov, V. I. Zhuravlev, G. S. Zaslavskii, M. V. Zakhvatkin, A. N. Zinov'ev, Y. Ilinen, A. V. Ipatov, B. Z. Kanevskii, I. A. Knorin, J. L. Casse, K. I. Kellermann, Y. A. Kovalev, Y. Y. Kovalev, A. V. Kovalenko, B. L. Kogan, R. V. Komaev, A. A. Konovalenko, G. D. Kopelyanskii, Y. A. Korneev, V. I. Kostenko, A. N. Kotik, B. B. Kreisman, A. Y. Kukushkin, V. F. Kulishenko, D. N. Cooper, A. M. Kut'kin, W. H. Cannon, M. G. Larionov, M. M. Lisakov, L. N. Litvinenko, S. F. Likhachev, L. N. Likhacheva, A. P. Lobanov, S. V. Logvinenko, G. Langston, K. McCracken, S. Y. Medvedev, M. V. Melekhin, A. V. Menderov, D. W. Murphy, T. A. Mizyakina, Y. V. Mozgovoi, N. Y. Nikolaev, B. S. Novikov, I. D. Novikov, V. V. Oreshko, Y. K. Pavlenko, I. N. Pashchenko, Y. N. Ponomarev, M. V. Popov, A. Pravin-Kumar, R. A. Preston, V. N. Pyshnov, I. A. Rakhimov, V. M. Rozhkov, J. D. Romney, P. Rocha, V. A. Rudakov, A. Räisänen, S. V. Sazankov, B. A. Sakharov, S. K. Semenov, V. A. Serebrennikov, R. T. Schilizzi, D. P. Skulachev, V. I. Slysh, A. I. Smirnov, J. G. Smith, V. A. Soglasnov, K. V. Sokolovskii, L. H. Sondaar, V. A. Stepan'yants, M. S. Turygin, S. Y. Turygin, A. G. Tuchin, S. Urpo, S. D. Fedorchuk, A. M. Finkel'shtein, E. B. Fomalont, I. Fejes, A. N. Fomina, Y. B. Khapin, G. S. Tsarevskii, J. A. Zensus, A. A. Chuprikov, M. V. Shatskaya, N. Y. Shapirovskaya, A. I. Sheikhet, A. E. Shirshakov, A. Schmidt, L. A. Shnyreva, V. V. Shpilevskii, R. D. Ekers, and V. E. Yakimov, ""RadioAstron"-A telescope with a size of 300 000 km: Main parameters and first observational results," *Astronomy Reports*, vol. 57, pp. 153–194, Mar. 2013.

[2] L. Association, "Radioastron reflector description,"

[3] R. F. C. Vessot, M. W. Levine, E. M. Mattison, E. L. Blomberg, T. E. Hoffman, G. U. Nystrom, B. F. Farrel, R. Decher, P. B. Eby, and C. R. Baugher, "Test of relativistic gravitation with a space-borne hydrogen maser," *Physical Review Letters*, vol. 45, pp. 2081–2084, Dec. 1980.

[4] D. A. Litvinov, U. Bach, N. Bartel, K. G. Belousov, M. Bietenholz, A. V. Biriukov, G. Cimo, D. A. Duev, L. I. Gurvits, A. V. Gusev, R. Haas, V. L. Kauts, B. Z. Kanevsky, A. V. Kovalenko, G. Kronschnabl, V. V. Kulagin, M. Lindqvist, G. Molera Calves, A. Neidhardt, C. Ploetz, S. V. Pogrebenko, N. K. Porayko, V. N. Rudenko, A. I. Smirnov, K. V. Sokolovsky, V. A. Stepanyants, J. Yang, and M. V. Zakhvatkin, "RadioAstron gravitational redshift experiment: status update," *ArXiv e-prints*, May 2016.

[5] O. Montenbruck and E. Gill, "Satellite orbits," *Springer*, vol. 2, pp. 257–291, 2000.

[6] A. V. Biriukov, V. L. Kauts, V. V. Kulagin, D. A. Litvinov, and V. N. Rudenko, "Gravitational redshift test with the space radio telescope "RadioAstron"," *Astronomy Reports*, vol. 58, pp. 783–795, Nov. 2014.

[7] EVN, "Radio observatories,"

[8] P. Delva, N. Puchades, E. Schönemann, F. Dilssner, C. Courde, S. Bertone, F. Gonzalez, A. Hees, C. Le Poncin-Lafitte, F. Meynadier, R. Prieto-Cerdeira, B. Sohet, J. Ventura-Traveset, and P. Wolf, "Gravitational redshift test using eccentric galileo satellites," *Phys. Rev. Lett.*, vol. 121, p. 231101, Dec 2018.

[9] S. Herrmann, F. Finke, M. Llf, O. Kichakova, D. Puetzfeld, D. Knickmann, M. List, B. Rievers, G. Giorgi, C. Gnther, H. Dittus, R. Prieto-Cerdeira, F. Dilssner, F. Gonzalez, E. Schnemann, J. Ventura-Traveset, and C. Lmmerzahl, "Test of the gravitational redshift with galileo satellites in an eccentric orbit," *Physical Review Letters*, vol. 121, 12 2018.

[10] K. V. Sokolovsky, "RadioAstron early science program space-VLBI AGN survey: strategy and first results," in *Proceedings of the 11th European VLBI Network Symposium Users*

Meeting. 9-12 October, 2012. Bordeaux (France). Online at ¡A href="http://pos.sissa.it/cgi-bin/reader/conf.cgi?confid=178"¿http://pos.sissa.it/cgi-bin/reader/conf.cgi?confid=178¡/A¿, id.109, p. 109, 2012.

[11] M. V. Zakhvatkin, Y. N. Ponomarev, V. A. Stepan'yants, A. G. Tuchin, and G. S. Zaslavskiy, "Navigation support for the RadioAstron mission," *Cosmic Research*, vol. 52, pp. 342–352, Sept. 2014.

[12] K. I. of Applied Mathematics, "Radio astron orbit determination data, reconstructed orbit,"

[13] J. B. Hartle, *Gravity: An introduction to Einsteins general relativity*. AAPT, 2003.

[14] D. Litvinov, V. Rudenko, A. Alakoz, U. Bach, N. Bartel, A. Belonenko, K. Belousov, M. Bietenholz, A. Biriukov, R. Carman, G. Cim, C. Courde, D. Dirkx, D. Duev, A. Filetkin, G. Granato, L. Gurvits, A. Gusev, R. Haas, G. Herold, A. Kahlon, B. Kanevsky, V. Kauts, G. Kopelyansky, A. Kovalenko, G. Kronschnabl, V. Kulagin, A. Kutkin, M. Lindqvist, J. Lovell, H. Mariey, J. McCallum, G. M. Calvs, C. Moore, K. Moore, A. Neidhardt, C. Pltz, S. Pogrebenko, A. Pollard, N. Porayko, J. Quick, A. Smirnov, K. Sokolovsky, V. Stepanyants, J.-M. Torre, P. de Vicente, J. Yang, and M. Zakhvatkin, "Probing the gravitational red-shift with an earth-orbiting satellite," *Physics Letters A*, vol. 382, no. 33, pp. 2192 – 2198, 2018. Special Issue in memory of Professor V.B. Braginsky.

[15] R. V. Pound and G. A. Rebka, "Gravitational red-shift in nuclear resonance," *Phys. Rev. Lett.*, vol. 3, pp. 439–441, Nov 1959.

[16] F. Meynadier, P. Delva, C. le Poncin-Lafitte, C. Guerlin, and P. Wolf, "Atomic clock ensemble in space (aces) data analysis," *Classical and Quantum Gravity*, vol. 35, no. 3, p. 035018, 2018.

[17] Y. Su, B. R. Heckel, E. G. Adelberger, J. H. Gundlach, M. Harris, G. L. Smith, and H. E. Swanson, "New tests of the universality of free fall," , vol. 50, pp. 3614–3636, Sept. 1994.

[18] P. Jetzer, "General relativity tests with space clocks in highly elliptic orbits," *International Journal of Modern Physics D*, vol. 26, p. 1741014, 2017.

[19] R. Reasenberg, J. Chandler, N. Colmenares, N. Johnson, T. Murphy, and I. Shapiro, "Modeling and analysis of the apollo lunar laser ranging data," *arXiv preprint arXiv:1608.04758*, 2016.

[20] S. W. Asmar, J. W. Armstrong, L. Iess, and P. Tortora, "Spacecraft Doppler tracking: Noise budget and accuracy achievable in precision radio science observations," *Radio Science*, vol. 40, p. RS2001, Apr. 2005.

[21] L. Blanchet, C. Salomon, P. Teyssandier, and P. Wolf, "Relativistic theory for time and frequency transfer to order c^{-3}," , vol. 370, pp. 320–329, Apr. 2001.

[22] M. Soffel, S. A. Klioner, G. Petit, P. Wolf, S. Kopeikin, P. Bretagnon, V. Brumberg, N. Capitaine, T. Damour, T. Fukushima, *et al.*, "The iau 2000 resolutions for astrometry, celestial mechanics, and metrology in the relativistic framework: explanatory supplement," *The Astronomical Journal*, vol. 126, no. 6, p. 2687, 2003.

[23] A. Hees, S. Bertone, and C. Le Poncin-Lafitte, "Relativistic formulation of coordinate light time, Doppler, and astrometric observables up to the second post-Minkowskian order," , vol. 89, p. 064045, Mar. 2014.

[24] L. Iess, M. Di Benedetto, N. James, M. Mercolino, L. Simone, and P. Tortora, "Astra: Interdisciplinary study on enhancement of the end-to-end accuracy for spacecraft tracking techniques," *Acta Astronautica*, vol. 94, pp. 699–707, Feb. 2014.

[25] B. et al., "Characterization of frequency stability," November 1970.

[26] B. Schutz, B. Tapley, and G. H. Born, *Statistical orbit determination*. Academic Press, 2004.

[27] D. A. Duev, G. M. Calvés, S. V. Pogrebenko, L. I. Gurvits, G. Cimo, and T. B. Bahamon, "Spacecraft vlbi and doppler tracking: algorithms and implementation," *Astronomy & Astrophysics*, vol. 541, p. A43, 2012.

[28] G. M. Calvs, *Radio spectroscopy and space science with VLBI radio telescopes for Solar System research*. PhD thesis, Aalto University, 2012.

[29] N., V., N. Nunes, M. Bartel, F., M. Bietenholz, V., D. Zakhavatkin, A., V. Litvinov, N., L. Rudenko, I., G. Gurvits, D. Granato, and Dirkx, "The gravitational redshift monitored with radioastron from near earth up to 350,000 km," (2018, under revision).